



Hot Compression Behavior and Microstructure Evolution of an Mg–Gd–Y–Zn–Zr Alloy Containing the 14H LPSO Phase with Different Morphologies

YUXIANG HAN, ZHIYONG CHEN, HAN CHEN, JINGYI HUANG,
and CHUMING LIU

In this paper, the microstructures with two different morphologies of intragranular lamellar 14H long-period stacking-ordered (LPSO) phase were designed in Mg–4.7Gd–3.4Y–1.2Zn–0.5Zr (wt pct) alloy, and their hot processing maps were established based on a series of hot compression tests. The deformation behavior and microstructure evolution of the two alloys during hot compression were investigated, the effect of 14H LPSO phase on dynamic recrystallization (DRX), texture, and hot workability also discussed. The alloy annealed at 400 °C (400AT alloy) with densely distributed 14H LPSO phase and the alloy annealed at 450 °C (450AT alloy) with sparsely distributed 14H LPSO phase has the approximate peak stress and activation energy values. However, the 400AT alloy offers a greater hot processing window than the 450AT alloy. With the compressive temperature increasing or the strain rate decreasing, 14H LPSO phase gradually changes from a metastable state to a stable state in 400AT alloys, while it gradually dissolves in 450AT alloy. In addition, necklace-shaped discontinuous dynamic recrystallization (DDRX) grains were mainly distributed around the original deformed grains, continuous dynamic recrystallization (CDRX) grains were primarily located in the kink boundary, triangular grain boundary and widely spaced LPSO phase lamella in both alloys. For the 450AT alloy, more 14H LPSO phase kink boundary and larger space between LPSO phase lamellae promotes to the formation of CDRX grains, while limit the texture weakening. The 400AT alloy exhibits a weaker texture intensity and more randomly distributed grain orientation, which was related to the existence of large amount of DDRX grains. The weaker basal texture was beneficial to the hot workability and well corresponding to the larger appropriate hot processing region of 400 AT alloy.

<https://doi.org/10.1007/s11661-023-07203-9>

© The Minerals, Metals & Materials Society and ASM International 2023

I. INTRODUCTION

AS the lightest metal structural materials, Mg alloys are widely used in aerospace, automotive, electronics, and other fields due to their advantages such as low density, high specific strength and stiffness, good thermal conductivity, good shock absorption, and excellent electromagnetic shielding.^[1,2] However, the tensile strength of commercially wrought Mg alloys currently

does not exceed 360 MP at room temperature, and the service temperature is mostly below 200 °C, which greatly limits their development and application.^[3] How to improve their room and elevated temperatures mechanical properties have become a burning issue to be solved.

Since 2001, the Mg₉₇Zn₁Y₂ alloy-containing long-period stacking-ordered (LPSO) phases with a tensile yield strength of 600 MPa and elongation of 5 pct at room temperature was produced by Kawamura *et al.* using rapidly solidified powder metallurgy processing.^[4] The existence of LPSO phases is considered to be beneficial for the strength, and the structure and strengthening mechanism of LPSO phases have received great attention. In particular, over the past decade, the Mg–RE (rare earth)–Zn series alloys containing LPSO phase have attracted extensive attention due to their excellent comprehensive mechanical properties. Therein, it is found that the addition of Gd and Y can significantly enhance the solid solution and aging strengthening

YUXIANG HAN, ZHIYONG CHEN, HAN CHEN, and JINGYI HUANG are with the School of Materials Science and Engineering, Central South University, Changsha 410083, P.R. China. Contact e-mail: czysh@netease.com CHUMING LIU is with the School of Materials Science and Engineering, Central South University and also with the Hunan Meiyu Science and Technology Co., Ltd., Yueyang 414000, P.R. China.

Manuscript submitted April 17, 2023; accepted September 7, 2023.

Article published online September 21, 2023

effects.^[5] Meanwhile, the addition of Zr can improve the volume fraction of LPSO phase and refined grains.^[6] Some research has also reported that the Mg–Gd–Y–Zn–Zr alloy with LPSO phase occupied an ultra-high strength.^[7,8] In this kind of alloy, LPSO phase can effectively increase the slip resistance of basal slips, thereby promoting the activation of non-basal slips.^[9] Ultimately, the strength and ductility of the Mg–Gd–Y–Zn–Zr alloys are significantly improved at the same time. Therefore, the Mg–Gd–Y–Zn–Zr alloys have an exciting potential for practical applications.

Traditional elevated temperature plastic deformations, such as rolling, extrusion, or forging are still often used to improve the mechanical properties of Mg alloys in practical industrial applications.^[10–12] On one hand, the severe plastic deformation processes are always limited by the laboratory platform and small-scale production.^[13] On the other hand, the conventional plastic deformation could easily and effectively enhance the strength of Mg alloys without diminishing ductility to compared with the complexity of rapidly solidified power metallurgy.^[14] On this foundation, it is necessary to obtain the processing regimes for Mg alloys and, thus, achieving excellent mechanical properties. The hot processing map, based on the theory of continuum mechanics and irreversible mechanics, was widely used to describe, and compare the hot workability of Mg alloys.^[15] However, for the Mg/LPSO alloy, many vacancies still exist in the research on plastic forming, and their deformation mechanism during plastic processing is not sufficiently clear. Therefore, issues related to the plastic deformation process of Mg/LPSO alloys should be clarified.

The hot deformation behavior of Mg alloys general includes the relationship between flow stress and deformation condition, deformation mechanism, and dynamic recrystallization (DRX) behavior, and usually studied by the uniaxial hot compression test. Therein, constitutive equations and hot processing map derived from true stress–strain curves are used to describe the relationship between flow stress and deformation condition. For the deformation mechanism, what is different from traditional Mg alloys is that the Mg–RE alloy-containing LPSO phases seem to be more prone to kink during deformation.^[16,17] Oñorbe *et al.*^[18] have reported that the kinking of LPSO phase could effectively release stress concentration and coordinate deformation in the Mg–Y_{2x}–Zn_x alloys during extrusion. In another research, it is also found that the pyramidal $\langle c + a \rangle$ slip and kink of LPSO phase could coordinate deformation together at elevated temperatures and high strain rates in Mg–2.5Zn–4Y alloy.^[19]

In addition, DRX is a very vital mechanism to tailor the microstructure and texture for Mg alloys during hot deformation. In particular of the research in Mg/LPSO alloy, DRX behavior is closely related to the LPSO phase and has attracted more attention of investigators. Previous studies have reported that the LPSO phase often appears at the grain boundaries in the form of a block-shaped or precipitates along the basal plane of the matrix with a plate-like shape.^[12,20] With the changing of alloy elements and heat treatments, different volume

fractions and morphologies of the intragranular LPSO phase are generally presented in the alloys.^[21] In terms of the common intergranular block LPSO phase and intragranular lamellar LPSO phase, it has reported that the block 18R LPSO phase with higher elastic modulus^[22] and micro-hardness^[23] can promote DRX through particle-stimulated nucleation (PSN) mechanism. Some researchers found that the morphology of the intragranular LPSO phase is identified as critical factor in affecting the microstructure evolution, deformation mechanism, as well as mechanical property of the wrought Mg alloys.^[18,24–26] Accordingly, it is a potential way to optimize the microstructure and the mechanical properties of Mg alloys by regulating the morphology of intragranular LPSO phase. Notably, the role of intragranular 14H LPSO phase relative DRX mechanism is still controversial. In previous work, the lamellar LPSO phases can hinder the motion of dislocation and migration of GBs, and the dislocation accumulation could not occur significantly, which was against the nucleation and growth of DRX.^[27] Some research also found that the lamellar 14H LPSO phases can delay the DRX behavior by forming kink bands and coordinate strain.^[28] However, in another research, it is suggested that plate-shaped 14H LPSO phases could stimulate DRX by PSN mechanism.^[29] To sum up, the morphology and distribution of intragranular 14H LPSO phase are crucial for the DRX behavior.

At present, some research have been conducted on the microstructure and mechanical properties of Mg–Gd–Y–Zn–Zr alloy. However, studies on the hot deformation behavior of the alloy are not comprehensive enough. Specifically, there lacks detailed microstructural evidence that correlates the intragranular lamellar LPSO phases with dislocations, and thereafter, with the DRX behavior. Meanwhile, the detailed relationship between DRX mechanisms and texture weakening is still ambiguous. A comprehensive understanding of the relationship among LPSO phase, DRX evolution, and texture evolution is critical to the design of hot-working processes. Therefore, based on previous studies, initial microstructure with different distribution and morphology of the intragranular lamellar LPSO phase was designed by regulating heat treatment regimes. The microstructure and hot deformation behavior during hot compression under different deformation conditions of the Mg–4.7Gd–3.4Y–1.2Zn–0.5Zr alloy were investigated in this work. Furthermore, the hot processing map is obtained by data analysis and calculation of the activation energy, which provides theoretical reference and experimental basis for understanding the relationship between microstructure and thermal mechanical parameters.

II. EXPERIMENTAL PROCEDURES

The tested material in this work is an extruded Mg–4.7Gd–3.4Y–1.2Zn–0.5Zr (wt pct) alloy sheet. For investigate the effect of intragranular 14H LPSO phase morphology on DRX and texture characteristics during hot compression test, two plates with dimensions of

120 mm × 75 mm × 12 mm along the extruded direction (ED) were cut from the sheet and homogenized at 510 °C for 16 hours. Subsequently, two kinds of annealed treatments were performed to obtain alloys containing obvious morphology differences of LPSO phase based on our previous work.^[30] One is annealed at 400 °C for 30 minutes named 400AT alloy, and the other is annealed at 450 °C for 24 hours named 450AT alloy.

Cylindrical samples were machined along the same direction with a diameter of 10 mm and a height of 12 mm along the transverse direction (TD) from the two as-annealed plates. The hot compression test was performed on a Gleeble-3500 thermal simulator tester. During compression, graphite sheets and lubricants (synthetic anti-blocking lubricants of nickel and graphite) were placed on both ends of the cylindrical sample to reduce friction with the indenter, which could optimize uneven deformation of the sample. The process parameters selected in the experiment mainly include deformation temperatures (350 °C, 400 °C, 450 °C, 500 °C) and strain rates (0.001 s^{-1} , 0.01 s^{-1} , 0.1 s^{-1} , 1 s^{-1}). During hot compression process, the sample was heated to the test temperature at the heating rate of 5 °C/s and then compressed after being held for 3 minutes. All samples were compressed to the total true strain of 0.5 and then immediately quenched in water to retain the high-temperature deformation microstructure. The experimental process is automatically controlled by

the computer, the parameters of pressure, true stress, true strain, displacement, temperature, and time are dynamically recorded.

The microstructure of the as-annealed and hot compression specimens was examined by optical microscopy (OM), scanning electron microscopy (SEM), electron back-scattered diffraction (EBSD), and transmission electron microscopy (TEM). OM and SEM samples were etched with solution of 4.2 g picric acid, 10 mL acetic acid, 10 mL distilled water, and 70 mL ethanol. Specimens for EBSD and TEM measurements were mechanical polished and then electropolished in a solution of 96 pct ethyl alcohol and 4 pct perchloric acid at − 35 °C. EBSD measurement was performed on the plane of compression direction (CD) with step sizes of 1.5 μm using HKL Technology Channel V acquisition system on a JSM-7900F SEM. FEI Titan G2 60-300 TEM operated at 300 kV was used to observe the LPSO phase and diffraction spots.

III. RESULTS

A. Initial Microstructures with Different Morphologies of LPSO Phase

Microstructure of the as-homogenized alloy consists of approximately equiaxed grains and exhibits a weak preferred orientation, as shown in Figure 1. In the EBSD map, the misorientation angle of grain

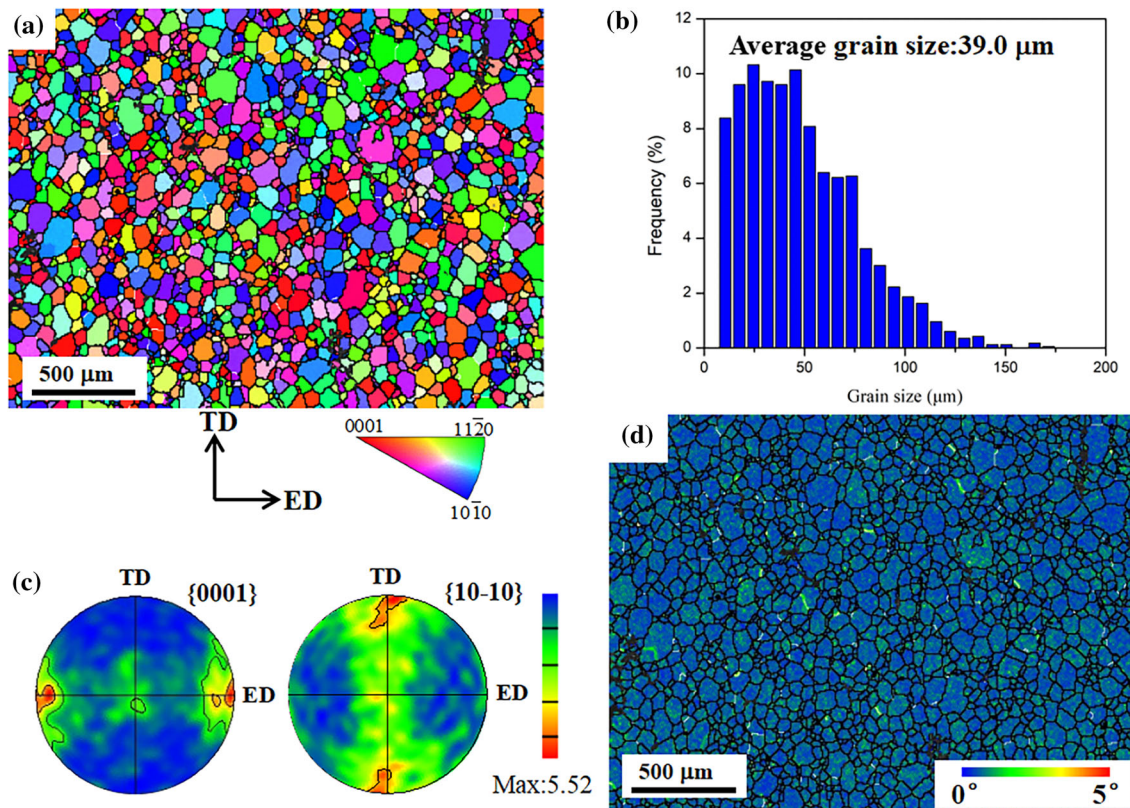


Fig. 1—Microstructure of as-homogenized alloy. (a) EBSD map colored relative to normal direction (ND). (b) grain size distribution map. (c) {0001} and {10-10} pole figures. (d) local misorientation distribution map (Color figure online).

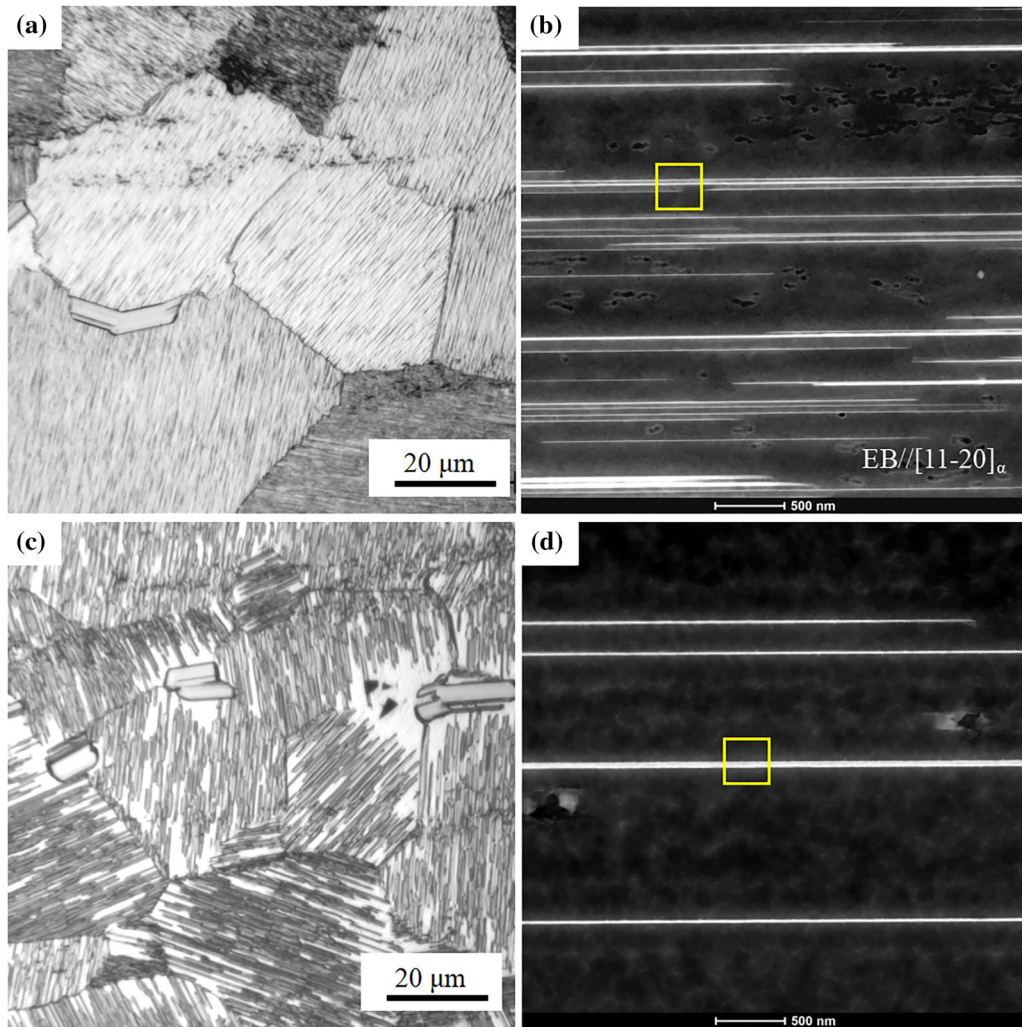


Fig. 2—Microstructures of the as-annealed alloys: (a, b) 400AT alloy; (c, d) 450AT alloy.

boundaries greater than 15 deg is represented by black lines and defined as high-angle grain boundaries (HAGBs), the misorientation angle in the range from 2 to 15 deg is represented by white lines and defined as low-angle grain boundaries (LAGBs).^[31] In fact, after 510 °C and 16 hours of solution treatment, the initial extruded alloys undergo complete static recrystallization, and it can be statistics from Figure 1(a) and (b) that the average grain size of approximately equiaxed grains encircled by HAGBs is 39 μm. From the pole figures in Figure 1(c), the alloy has a weak preferred orientation, and the maximum texture intensity is only 5.52. In Figure 1(d), the local misorientation distribution map reveals that there is almost no deformed structure in the as-homogenized alloy. Therefore, the study can eliminate the disturbance of initial deformed microstructure.

The microstructure with two different annealing regimes is shown in Figure 2. The precipitates in both alloys mainly consist of the block-shaped LPSO phase sporadically distributed on the grain boundaries and the lamellar LPSO phase massively distributed in the grain interior.^[32] A main difference in LPSO phase

morphology between the two alloys is that the intragranular lamellar LPSO phase in the 450AT alloy is coarser and more distributed more sparsely than that in the 400AT alloy, as shown in the SEM images (a, c) and STEM images (b, d), respectively. It is worth noting that due to the short time of solution treatment, the number of block-shaped precipitates is very small, and the size is also small, so their effect on the microstructure and hot deformation behavior can be ignored in the manuscript. By careful observation, some LPSO phase-free zones are frequently observed near the grain boundaries in the 450AT alloy. The formation of such zones is attributed to the increased solid solubility of RE elements with the increase of annealing temperature from 400 °C to 450 °C further shortening the length of lamellar LPSO phase.^[30] In addition, the mean grain size of 400AT alloy and 450AT alloy is 41.3 and 43.6 μm measured by mean linear intercept method, which is approximately that of as-homogenized alloy. It has reported that the dense and homogeneous intragranular 14H LPSO phases can effectively hinder the migration of grain boundary and restrict the lattice rotation of the α-Mg grains.^[12] Therefore, the difference in grain size between

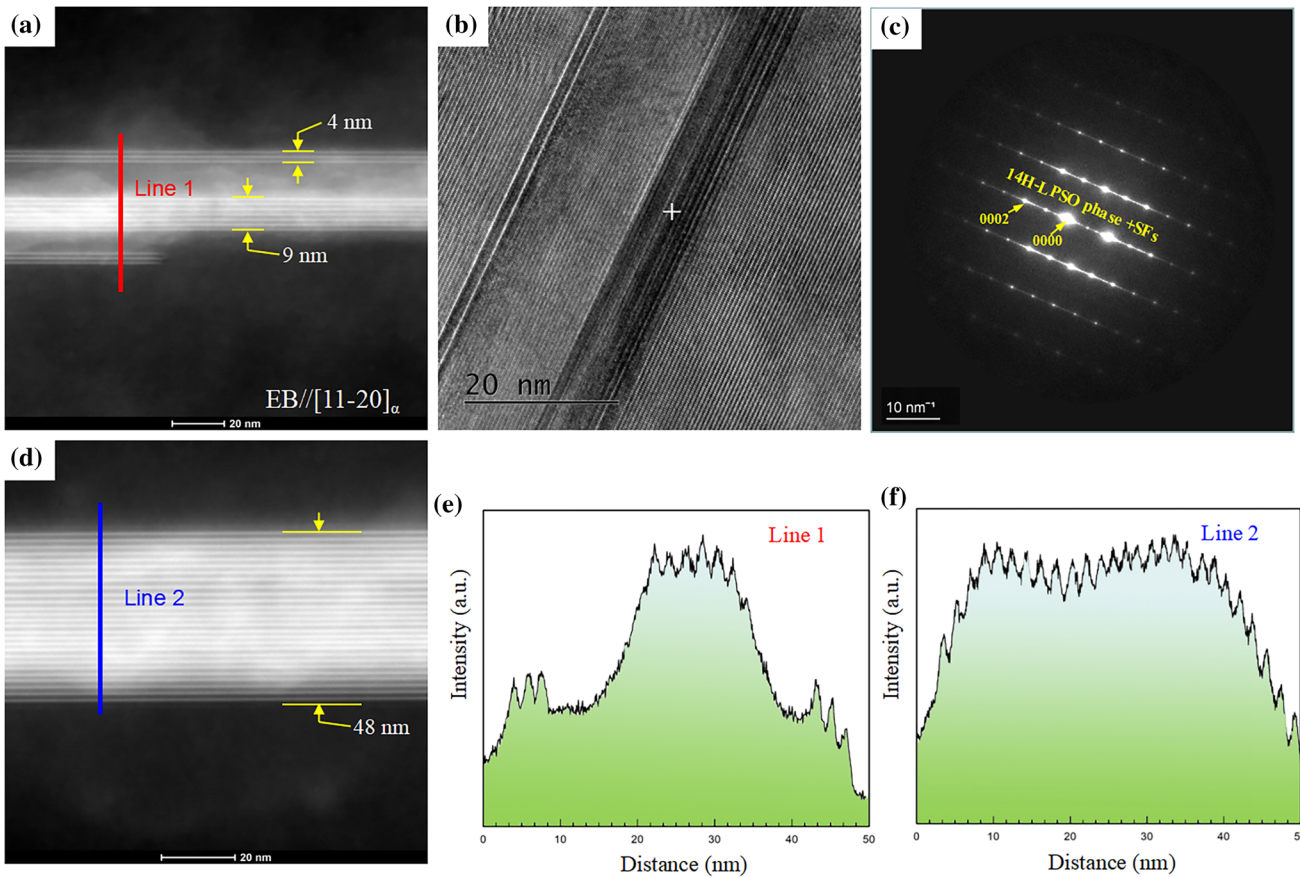


Fig. 3—TEM observation for the morphology and structure of LPSO phase. (a) HAADF-STEM observation for the LPSO phase in 400AT alloy. (b) HRTEM images of the LPSO phase in 400AT alloy. (c) SAED patterns of LPSO phase in 400AT alloy. (d) HAADF-STEM observation for the LPSO phase in 450AT alloy. (e) and (f) The interlayer spacing of the LPSO-building block in 400AT and 450AT alloy, respectively.

the two alloys is small and can be ignored in this study. This also excludes the influence of grain size on subsequent compression.

The morphological differences of LPSO phase in two alloys are further investigated by the high-angle annular dark field scanning transmission electron microscopy (HAADF-STEM), and the results are presented in Figure 3. A specific type of LPSO phase is constituted by fundamental ABCA building blocks and matrix layers with a constant number.^[33] The B and C layers of ABCA building blocks show bright contrast due to the enrichment of Zn/Gd/Y atoms, and the magnesium matrix layers present dark contrast as observed by HAADF-STEM. As shown in Figure 3(a) and (b), lamellar LPSO phase with different thicknesses is observed in 400AT alloy, the spacing of bright stripes is not a constant value, which means that the phase is metastable LPSO-building block clusters.^[34] In addition, in the corresponding SAED pattern of Figure 3(c), 13 diffraction spots with some streaks parallel to the $(0002)_z$ are detected between $[0001]_z$ and $[0002]_z$ spots, indicating that the phase has a 14H LPSO structure. In addition, these streaks in the SAED pattern indicate the formation of SFs.^[35] However, for the LPSO phase in 450AT alloy, the lamella thickness is more homogeneous, and the spacing of bright stripes becomes

identical, as shown in Figure 3(d). Based on the above research,^[30] it can be known that the metastable LPSO phases are gradually transformed into the stable 14H LPSO phase after long-time annealing. Figure 3(e) and (f) shows the distribution results of HAADF-STEM and layer spacing of different forms of LPSO phases in the above two alloys, respectively. For the LPSO phase in Figure 3(a), the spacing difference is large (as shown in line 1), which means that the lamella has not formed a regular LPSO phase-stacking structure. Therefore, the lamellar phase in 400AT alloy is mainly composed of metastable 14H LPSO phase and stacking faults. However, for the LPSO phase in Figure 3(d), the spacing of most bright stripes is approximately the same and close to 1.8 nm (as shown in line 2), and it can be considered that the type of LPSO phase is stable 14H structure.^[36]

B. Hot Compressive Deformation Behavior

Figure 4 shows the flow stress–strain curves of the 400AT alloy (full line) and 450AT alloy (dotted line) under different strain rates and deformation temperatures during hot compression. The universal characteristics of the stress–strain curves are similar at all deformation conditions, and three distinct regions are presented on the curves. These regions generally

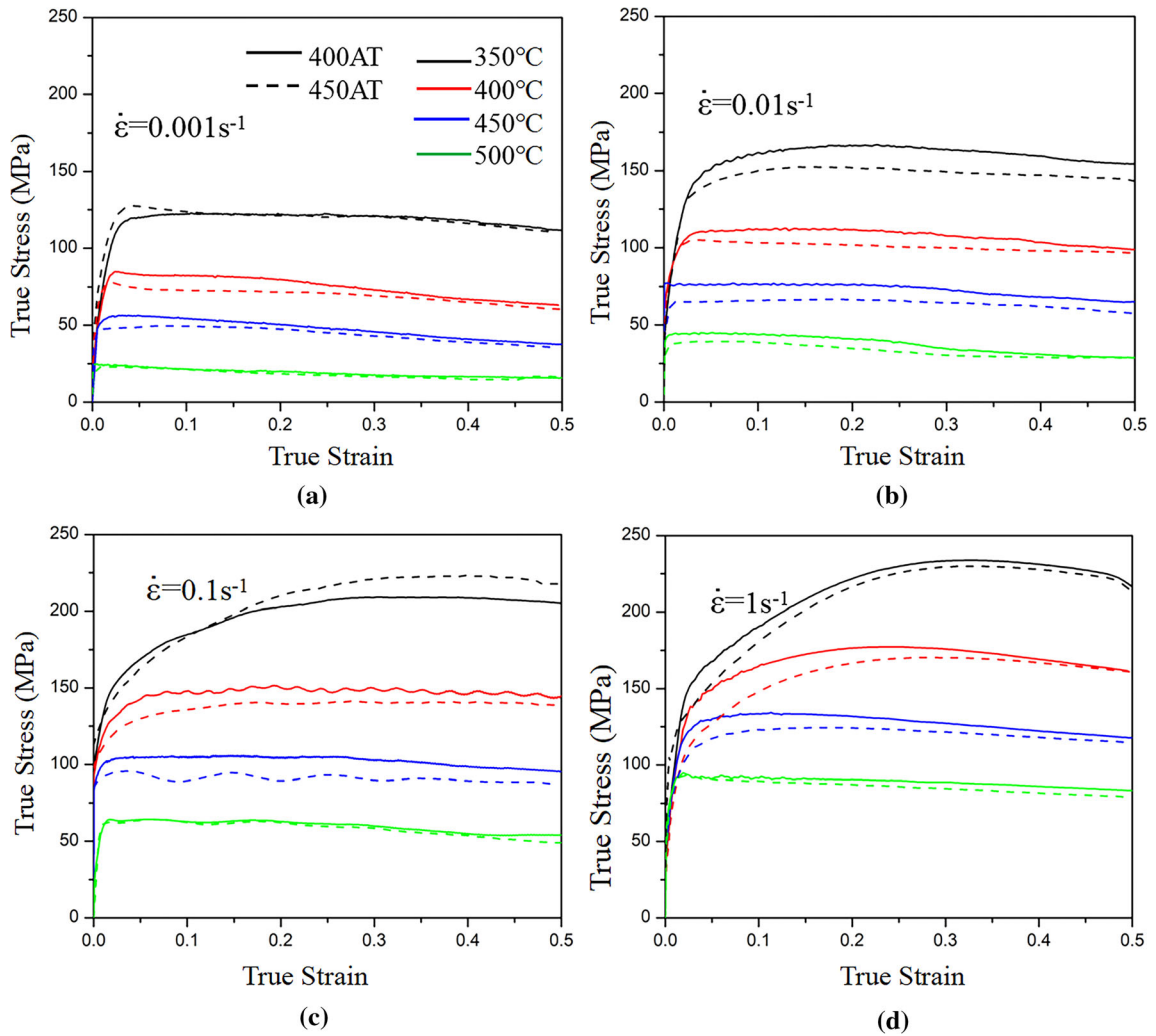


Fig. 4—True stress–strain curves of 400AT alloy and 450AT alloy during hot compression at different conditions: (a) 0.001 s^{-1} , (b) 0.01 s^{-1} , (c) 0.1 s^{-1} , and (d) 1 s^{-1} .

represent three distinct stages, which are hardening stage, transition stage, and softening stage. In the initial stage, the flow stress increases with increasing strain, which is due to the work hardening caused by the increase in dislocation density. In the transition stage, the softening effect introduced by DRX can eliminate the work-hardening effect, and the stress gradually increases to the peak value. The corresponding peak stress value decreases with increasing temperature or decreasing strain rate in the two alloys, as shown in the histogram of Figure 5.

Notably, none of these curves in Figure 4 exhibit a significant peak characteristic. Sun *et al.*^[37] have reported that dislocations in the grain hardly accumulate due to the sufficient dynamic recovery, which results in an imperceptible peak stress in these curves. In other words, the typical continuous DRX (CDRX) mechanism may dominate the DRX process in the two alloys during hot compression.

Additionally, it is worth noting that a serrated stress–strain curve presented in the 400AT alloy compressive at $400 \text{ }^\circ\text{C}$ and 0.1 s^{-1} , while occurs in the

450AT alloy during $450 \text{ }^\circ\text{C}$ and 0.1 s^{-1} compression. This phenomenon is like the Portevin–Le Chatelier (PLC) effect in Al alloys,^[38] and rarely found in the Mg–RE–Zn alloys. For the 400AT alloy, the metastable 14H LPSO phase gradually changes into a stable state and is accompanied by the diffusion of solute atoms (Gd/Y/Zn atoms) during $400 \text{ }^\circ\text{C}$ compressions. When the diffusion speed of atoms cannot keep up with the speed of movable dislocations with the increases of strain, the dislocations are repeatedly pinned and unlocked by solute atoms, thus, forms the serrated curve. For the 450AT alloy, the 14H LPSO phase can gradually be re-dissolved into the α -Mg matrix during $450 \text{ }^\circ\text{C}$ compressions with PLC effects. However, the fluctuation frequency is lower than that in the 400AT alloy due to the relatively elevated temperature stability of the LPSO phase.

Based on the above true stress–strain curve, determining an appropriate processing window is crucial for the hot deformation of alloy. In this study, the hot processing map at strain 0.4 consists of energy dissipation diagram (colorful map) and instability diagram

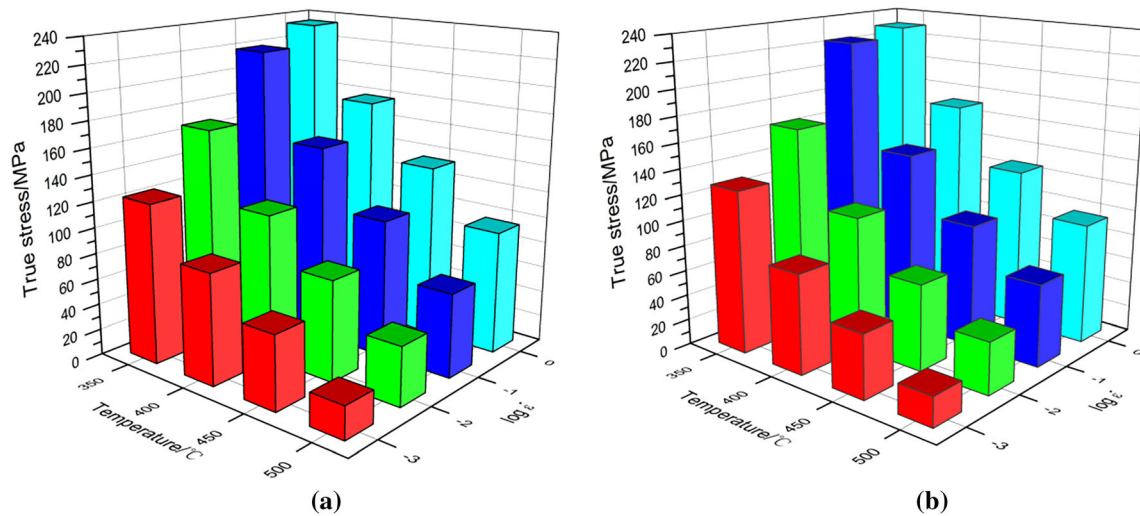


Fig. 5—Peak stress of the two alloys deformed at different conditions: (a) 400AT alloy; (b) 450AT alloy.

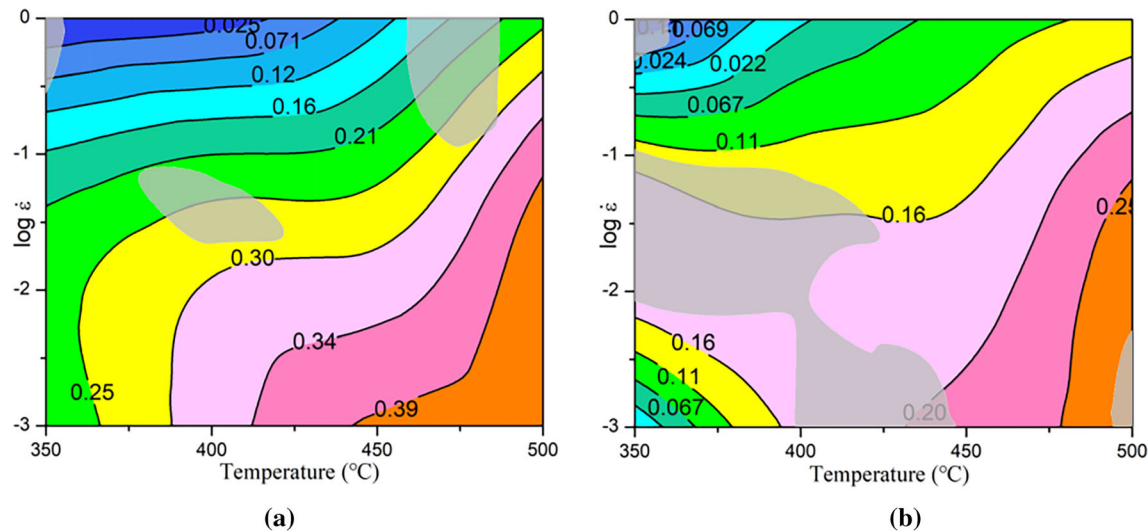


Fig. 6—Hot-processing map at 0.4 strain: (a) 400AT alloy, (b) 450AT alloy (Color figure online).

(gray shadow map) is used to compare and explore the proper deformation conditions of 400AT and 450AT alloy, as shown in Figure 6. Therein, the gray region represents the instability region, and the value of contour line represents the energy dissipation rate. Under the condition that stability is guaranteed, the higher the energy dissipation rate, the more suitable the material is for processing in this region.^[39] In addition, the activation energy (Q) is a crucial factor in the process of drawing hot processing map. The Q is defined as the threshold that must be overcome for nucleation and growth of new DRX grains^[30] and introduced to judge the difficulty of hot deformation. According to detailed calculation methods have been described in many studies,^[27,40] the obtained average Q value is calculated as 254.2 kJ/mol for 400AT alloy and 257.7 kJ/mol for 450AT alloy, which is much lower than that in other Mg/LPSO alloys.^[30,41] Besides, the

approximate and relatively low Q value suggests that both two alloys are relatively easier to deform at elevated temperatures. It can be seen that the highest energy dissipation rate region is located in the bottom right corner of both alloys. However, the 400AT alloy has a higher energy dissipation rate (0.39) than the 450AT alloy (0.25), and part of the instability region overlaps with the highest energy dissipation rate region in 450AT alloy, as shown in the bottom right corner of Figure 6(b). This should be attributed to the growth of DRX grains and variation of LPSO phase morphology. The detailed analysis will be discussed in the latter section.

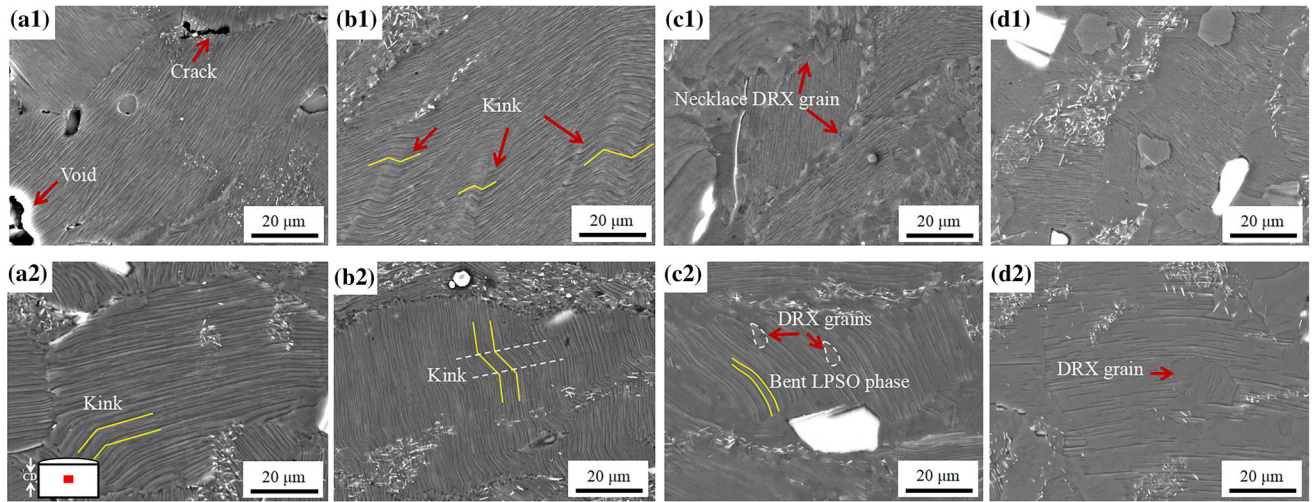


Fig. 7—SEM images of the two alloys compressive at 0.001 s^{-1} and different temperatures: (a₁) through (d₁) 350 °C to 500 °C of 400AT alloy. (a₂) through (d₂) 350 °C to 500 °C of 450AT alloy.

C. Microstructure Evolution Under Compression at Different Temperatures

The micromorphology of 400AT and 450AT alloy with different temperatures at the strain rate of 0.001 s^{-1} is shown in Figure 7. As shown in Figure 7(a₁), it can be clearly observed that some cracks and voids appear in the 400AT alloy with metastable 14H LPSO phase but not in 450AT alloy under 350 °C compression. This is attributed to the stable 14H LPSO phase itself can effectively release stress concentration through kink deformation (Figure 7(a₂)), thereby accommodating more strain. When the compression temperature reaches 400 °C, some kink bands are gradually revealed in the 400AT alloy (marked with yellow broken lines). Notably, it has reported that the intragranular 14H LPSO phase is always parallel to the $[0001]_z$ direction of grain,^[30] and the kink angle of the 14H LPSO phase is significantly different from the common twin misorientation angle of Mg alloys. Thus, in this case, the deformation of 14H LPSO phase is performed by the kink mechanism and not by twinning. In addition, on the one hand, the increase in temperature promotes the activation of more slip systems. On the other hand, the metastable LPSO phase gradually evolved into stable 14H LPSO phase, resulting in the occurrence of kinking and consistent with the PLC phenomenon in Figure 4(c). Notably, with the compression temperature further increases, some DRX grains decorated the initial deformed grain boundaries in 400AT alloy, exhibiting a typical necklace structure (Figure 7(c₁)). Liu *et al.*^[15] have demonstrated that the necklace structure is originate from the discontinuous dynamic recrystallization (DDRX) mechanism in Mg–Zn–Yb–Zr alloy. Therefore, in this situation, the stress concentration caused by

compression cannot be released through the kink of stable 14H LPSO phase, thereby using DDRX mechanism to form the necklace DRX grain structure around the deformed grains. In contrast, the LPSO phase lamellar spacing gradually increases with the temperature increases through re-dissolution mechanism in 450AT alloy (Figure 7(c₂)), and some DRX grain emerged between the lamella space. With further increasing the compression temperature, the 14H LPSO phase in both of alloys gradually shortens or even dissolves accompanied by DRX grains growth, as shown in Figures 7(d₁) and (d₂).

For further clarify the microstructure evolution of the two alloys at different compression temperatures, Figures 8 and 9 give the orientation maps, misorientation angle distribution maps, and kernel average misorientation (KAM) distribution maps of 400AT alloy and 450AT alloy compressive at 350 °C to 500 °C and 0.001 s^{-1} , respectively. The EBSD maps are colored relative to compression direction (CD). Obviously, both alloys show a typical bimodal microstructure after compression. With the compression temperature increases, the initial deformed grains are gradually consumed by growing DRX grains. Meanwhile, the change tendency of KAM value is consistent with LAGBs frequency in both of alloys. However, there is still a difference in the DRX grains fraction between the two alloys. The specific DRX fraction, average DRX grain size, and geometrically necessary dislocation density (ρ_{GND}) tendency are shown in Figure 10. Therein, the fraction of DRX grains is calculated based on the grain orientation spread (GOS) range from 0 to 2 deg, and the ρ_{GND} is calculated through KAM values.^[42,43] It is worth noting that the DRX fraction

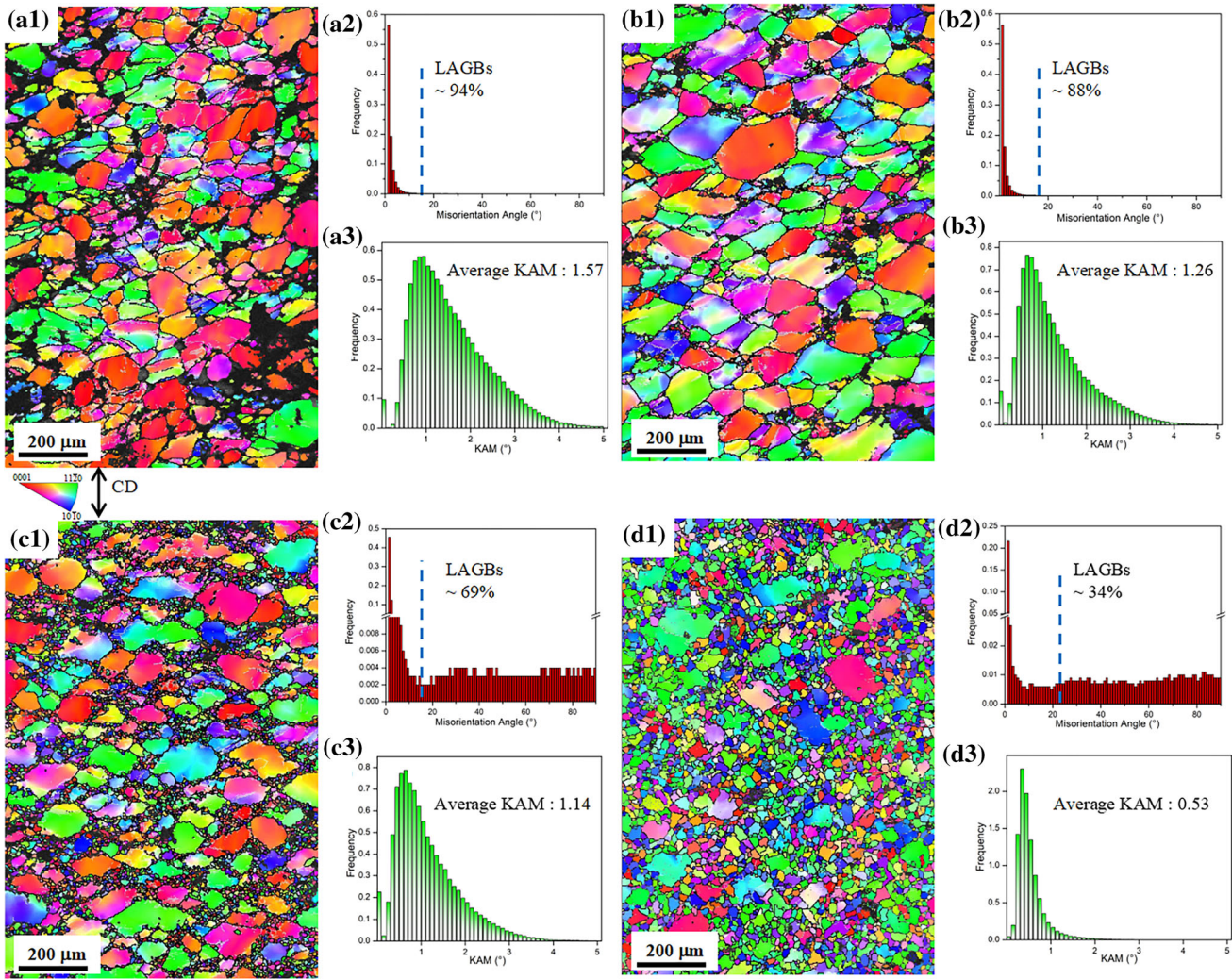


Fig. 8—Orientation maps, misorientation angle, and KAM value distribution of the 400AT alloy deformed at strain rate of 0.001 s^{-1} and different temperatures: (a₁) through (a₃) 350 °C, (b₁) through (b₃) 400 °C, (c₁) through (c₃) 450 °C, (d₁) through (d₃) 500 °C (Color figure online).

and ρ_{GND} in 400AT alloy are higher than those in 450AT alloy during the range of 450 °C to 500 °C compression, which may relate to the different DRX mechanism introduced by different LPSO morphology.

D. Microstructure Evolution Under Compression at Different Strain Rates

Like deformation temperature, strain rate also plays a significant role in regulating the DRX process and refining microstructures of deformed alloys. Figure 11 shows the SEM microstructures of the two alloys deformed at 500 °C and different strain rates. Under the relatively high compression temperature of 500 °C, the 14H LPSO phase gradually shortens or re-dissolves as the strain rate decreases, and numerous DRX grains are emerged in the microstructure in both of alloys.

Interestingly, unlike the 400AT alloy, kink deformation of the LPSO phases can still be observed at strain rate of 1 s^{-1} in 450AT alloy, and some DRX grains are nucleation at the kink boundary (Figure 11(a₂)). At the same time, some other DRX grains are distributed between the lamellar space of LPSO phase at strain rate of 0.01 s^{-1} in 450 AT alloy (Figure 11(c₂)), which is quite different from the 400AT alloy.

Figures 12 and 13 also reveal the orientation maps, misorientation angle, and KAM value distribution of 400AT alloy and 450AT alloy deformed at 500 °C and different strain rate, respectively. The orientation maps are colored relative to compression direction. It can be seen that with the compression strain rate decreases, the fraction of DRX grains increased in the two alloys. Also, the change tendency of KAM value is consistent with LAGBs frequency in both alloys. Figure 14 gives

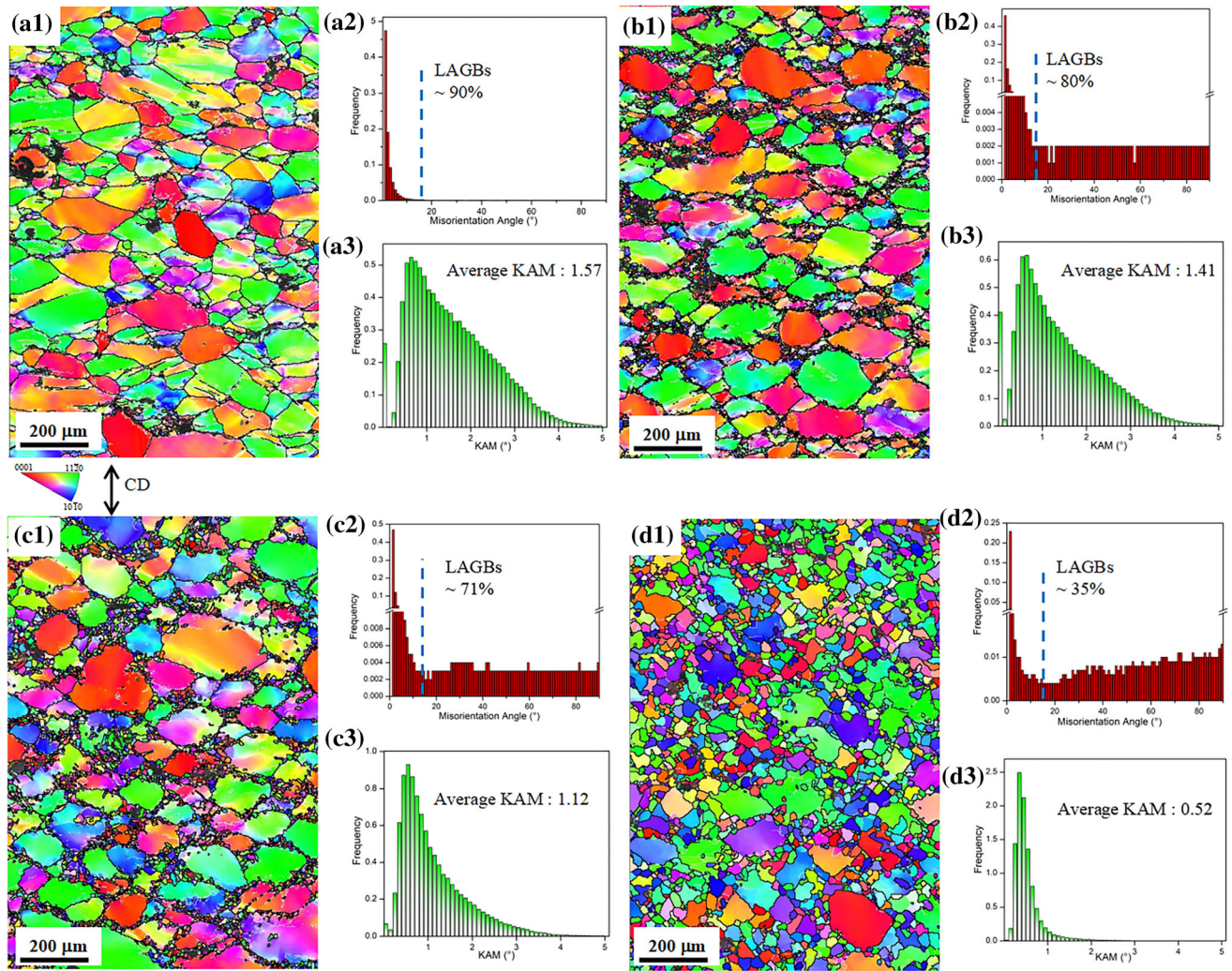


Fig. 9—Orientation maps, misorientation angle, and KAM value distribution of the 450AT alloy deformed at strain rate of 0.001 s^{-1} and different temperatures: (a₁) through (a₃) 350 °C, (b₁) through (b₃) 400 °C, (c₁) through (c₃) 450 °C, (d₁) through (d₃) 500 °C (Color figure online).

the trends of DRX fraction, average DRX grain size, and ρ_{GND} of the two alloys deformed at 500 °C and different strain rates. By careful comparison, the ρ_{GND} of 400AT alloy is almost always higher than that of 450 AT alloy, while the average DRX grain size is almost always lower than that of 450 AT alloy. This may relate to the inhibition effect of 14H LPSO phase on DRX.^[27] However, the DRX fraction of 450AT alloy is higher than that of 400AT alloy in 0.001 s^{-1} , which can be explained by the secondary deformation after DRX grain growth.

IV. DISCUSSIONS

A. Deformation Mechanism

It is widely known that introducing the LPSO phase into the Mg alloys can change the stacking faults energy of the Mg matrix, which result in the activation of multiple slip systems, especially the non-basal slips. For investigating the effect of LPSO phase morphologies on deformation mechanism during compression, in-grain misorientation axis (IGMA) analysis was adopted to clarify the primary slip mode of deformed grains in the two alloys. Chun *et al.*^[44] refer that orientation changes inside deformed grains are caused by slight lattice rotation with the activation of slip systems. Therefore, IGMA analysis is an experimental approach to identifying the activated slip system by matching the in-grains misorientation axis with the Taylor axis of a given slip mode. In this study, the formation of grain boundaries

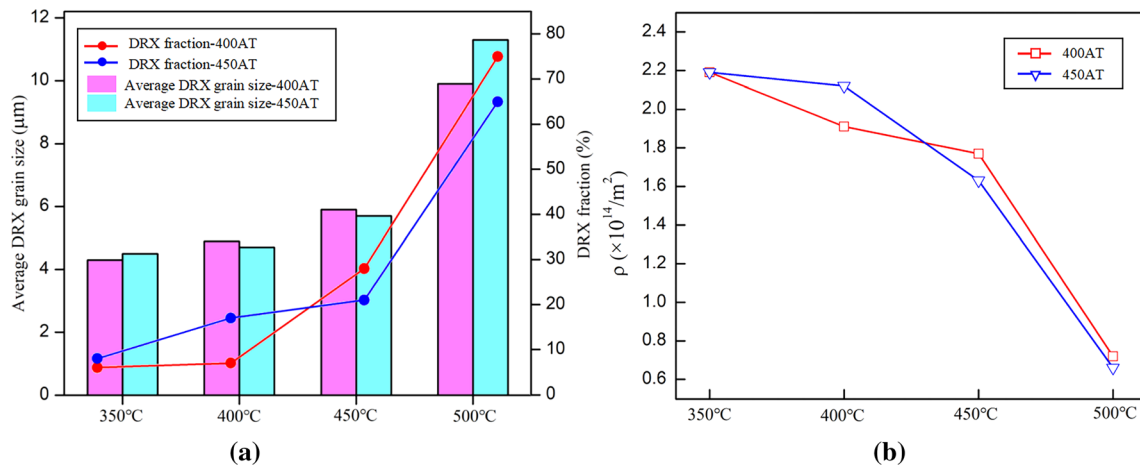


Fig. 10—The tendency of (a) DRX fraction and average DRX grain size, (b) GND density of the two alloys deformed at strain rate of 0.001 s^{-1} and different temperatures.

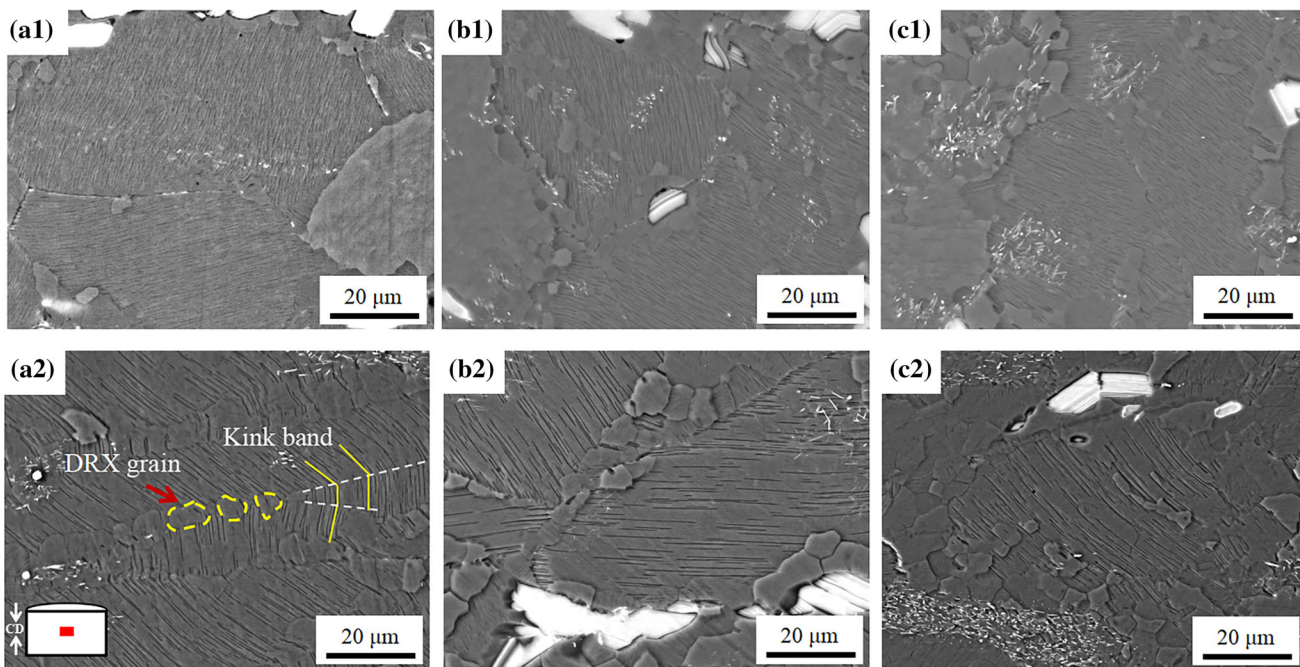


Fig. 11—SEM images of the two alloys compressive at $500 \text{ }^\circ\text{C}$ and different strain rates: (a₁) through (c₁) 1 s^{-1} through 0.01 s^{-1} of 400AT alloy, (a₂) through (c₂) 1 s^{-1} through 0.01 s^{-1} of 450AT alloy.

above 5 deg is usually accompanied by the formation of deformation bands that is kink band of LPSO phase.^[45] Therefore, the misorientation axis between 2 and 5 deg is plotted to investigate the slip mode, and a misorientation angle between 5 and 15 deg is plotted to explore the kink type.

The two alloys compressive at $400 \text{ }^\circ\text{C}$ and 0.001 s^{-1} were chosen to discuss the slip or kink mode due to the obvious presence of kink bands and to minimize the influence of DRX mechanism. The complete deformed grains with significant color changes are selected from the two alloys, as shown in Figures 15 and 16. In the 400AT alloy, it can be seen that the misorientation axis of selected grains 1 to 7 is primarily distributed at $\langle uv\bar{t}0 \rangle$

axes (*i.e.*, $\langle -12-10 \rangle$ to $\langle 01-10 \rangle$) and the maximum intensity (MI) larger than 2.0 m.u.d. , suggesting that both basal slip and the pyramidal slip may be preferentially activated in the deformed grains, as shown in Figure 15(a). For the grains 8 to 15 with misorientation angle between 5 and 15 deg shown in Figure 15(b), the IGMA is also concentrated near at $\langle uv\bar{t}0 \rangle$ axes, which demonstrate that the primary kink mode is basal kink.

However, in Figure 16(a) of 450AT alloy, unlike the 400AT alloy, misorientation axis in some selected grains (grain 3, 5, 6, 11, and 13) is concentrated near $\langle 0001 \rangle$ direction, and the MI is also greater than 2.0 m.u.d. , which matches the Taylor axis $\langle 0001 \rangle$ of the prismatic slip $\{01-10\}\langle -2110 \rangle$. It meant that prismatic slip should

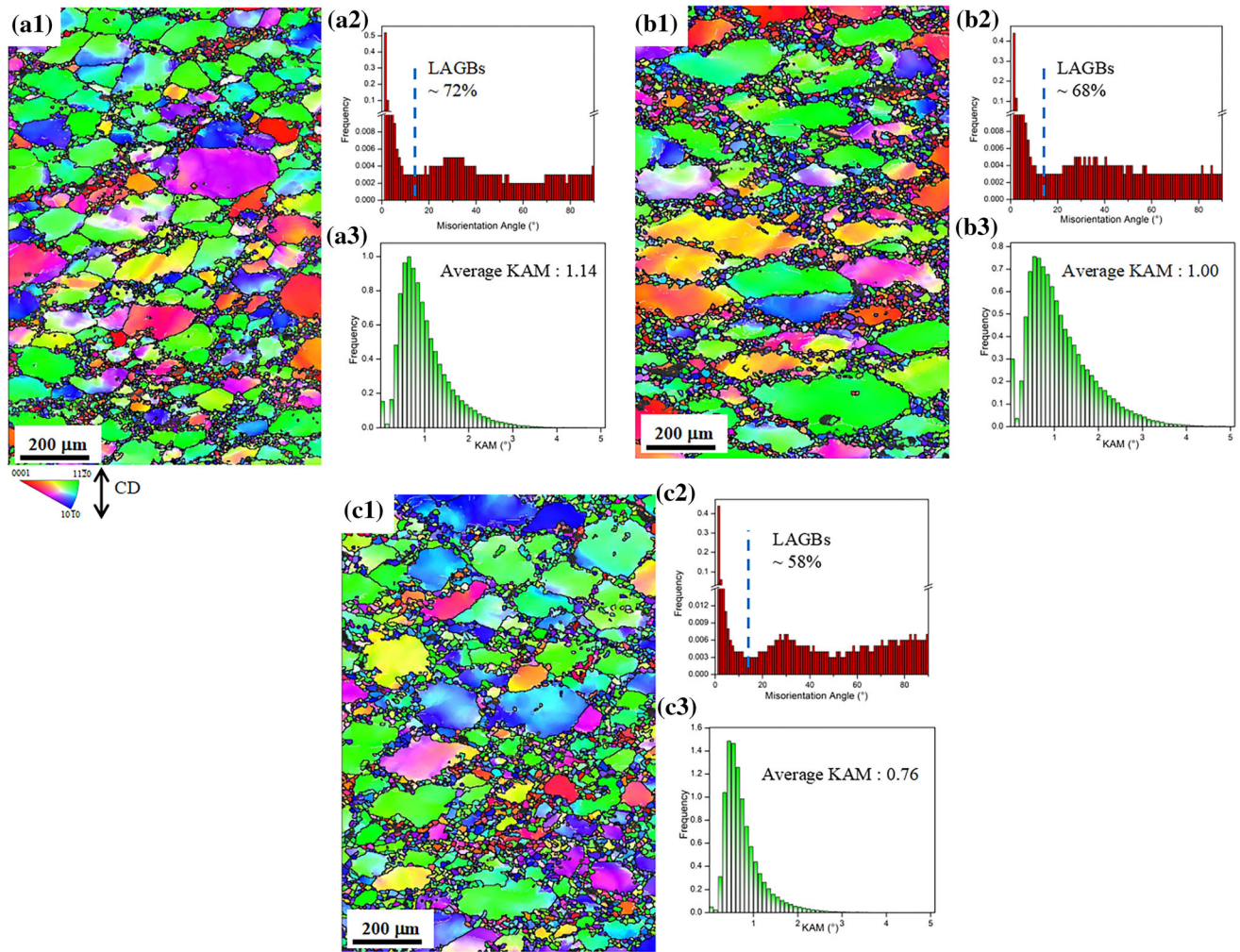


Fig. 12—Orientation maps, misorientation angle, and KAM value distribution of the 400AT alloy deformed at 500 °C and different strain rate: (a₁) through (a₃) 1 s⁻¹, (b₁) through (b₃) 0.1 s⁻¹ 400 °C, (c₁) through (c₃) 0.01 s⁻¹ (Color figure online).

be coactivated with basal slip or pyramidal slip in the alloy. In addition, the basal kink also plays a key role during compression, as shown in Figure 16(b) and grains 15 to 19. Shao *et al.*^[46] believe that the formation of basal kink originated from the basal slip or grain rotation, and before that, the basal slip was in an unfavorable orientation. It is also revealed that the density distributed 14H LPSO phase prevent the movement of non-basal slip to some extent, while the wide space of 14H LPSO phase lamellae contributes to more activation of prismatic or pyramidal slip.^[47]

B. DRX Mechanism

According to the above results, it can be obtained that the various microstructures with different morphologies and distribution of 14H LPSO phases show significantly distinct deformation behaviors, which is closely related to the different DRX mechanisms during compression. In order to better investigate the DRX mechanism presented in this study, Figure 17 provides two enlarged regions containing typical DRX grains formed at different sites of 450AT alloy during compression.

At first, Figure 17(a) reveals the typical kink 14H LPSO phase in 450AT alloy during 400 °C and 0.001 s⁻¹ compression. By careful observation, a series of fine DRX grains distributed at the kink boundary, and deformed grains M₁ and M₂ on both sides of the kink boundary activate the basal and prismatic slip (Figure 17b), which is consistent with the slip mode in Figure 16(b). It is worth mentioning that the angle between the grain *c*-axis on both sides of the kink boundary is significantly different from the twin misorientation angle; thus, the deformation mode of the 14H LPSO phase is kink rather than twinning. Meanwhile, the matrix near kink boundary shows some LAGBs attributed to the dislocation accumulation (Figure 17c). Zheng *et al.*^[48] concluded that LPSO phase was difficult to hinder the movement of basal slip due to its parallel to (0001). However, after kink deformation, the emergence of kink boundary can limit the basal slip, and LPSO phase hinders the movement of non-basal slip. Therefore, a higher strain distribution is exhibited near the kink boundary. Combined with the misorientation analysis of line AB (Figure 17i), the cumulative misorientation (point to origin) exhibits a larger orientation

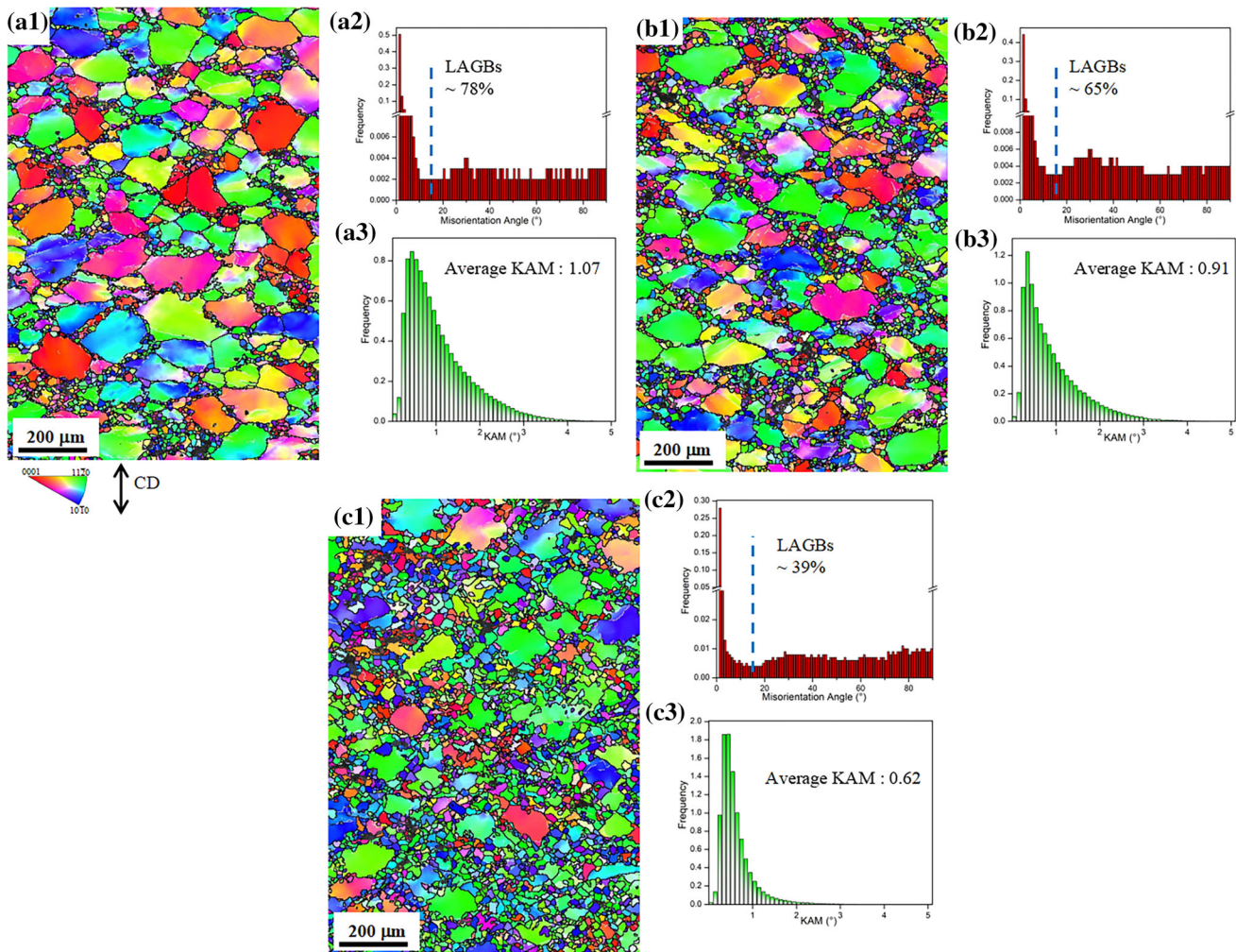


Fig. 13—Orientation maps, misorientation angle, and KAM value distribution of the 450AT alloy deformed at 500 °C and different strain rate: (a₁) through (a₃) 1 s⁻¹, (b₁) through (b₃) 0.1 s⁻¹ 400 °C, (c₁) through (c₃) 0.01 s⁻¹ (Color figure online).

gradient, which means the occurrence of sub-grains rotation and formation of HABSs originate from LAGBs. Therefore, the formation of fine DRX grains located in the kink boundary is attributed to the CDRX mechanism.^[46] In addition, the {0001} scattered data of CDRX grains in Figure 17(d) show that the orientation of DRX grains (black dashed rectangular area) is relatively concentrated near CD, as well as the deformed grains M₁ and M₂, indicating its limited weakening texture effect.

Figure 17(e) is the enlarged region belonging to 450AT alloy compressive at 450 °C and 0.001 s⁻¹. In this region, it is obvious that the bent lamellar LPSO phase of dense and sparse distributions coexist. By combining the orientation map of Figure 17(f), a large amount of DRX grains aggregate in the triangular grain boundaries. These DRX grains are nucleated by the stimulation of residual block phase at grain boundaries with PSN mechanism. During compression, numerous dislocations were piled up around the block phase, resulting in dislocation cells formed in the vicinity of block phase. With the strain increase, these cells gradually absorb surrounding dislocations thereby

forming the DRX grains, which is well according to the CDRX mechanisms. The typical CDRX grains located in the triangular grain boundaries are also often found in other Mg alloys.^[49]

However, other fine DRX grains decorated the deformed grain boundaries, exhibiting a typical necklace structure (grains P₁ through P₁₄). According to the KAM map of Figure 17(g), the local strain and high-level concentration of dislocations around the grain boundary bulges are indicated by red arrows. Meanwhile, the misorientation analysis of line CD (Figure 17(j)) and line EF (Figure 17(k)) also reveals the cumulative misorientation (point to origin) exhibits a small orientation gradient, and the point-to-point misorientation values remain lower than 2 deg, which is consistent with the DDRX characteristics. It means the occurrence of sub-grains rotation and formation of HABSs originate from LAGBs. In this situation, high local strain near the grain boundary contributes to the bulges and the DDRX grain nucleation is related to the migration of HAGBs.^[50] In addition, the {0001} scattered data of necklace DDRX grains in Figure 17(h) shows that the orientation of these grains is more

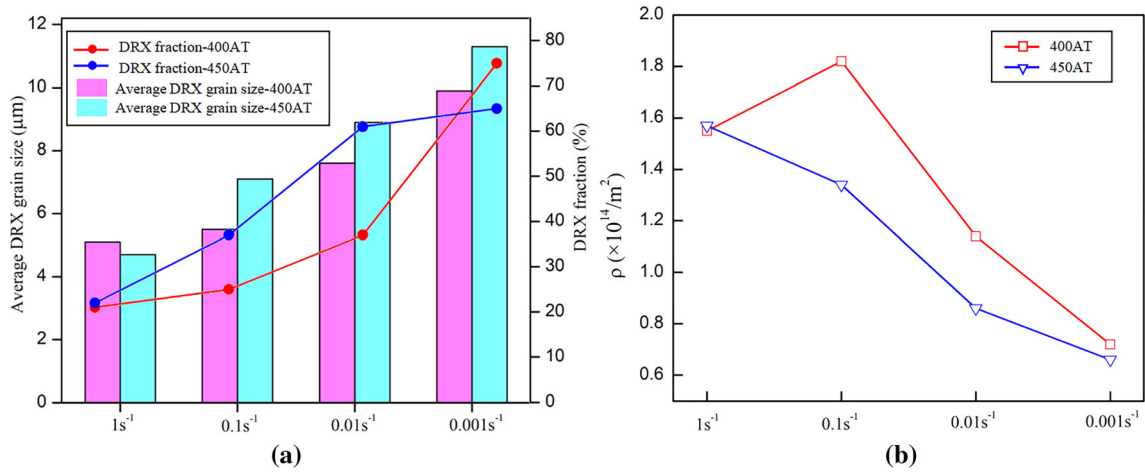


Fig. 14—The tendency of (a) DRX fraction and average DRX grain size, (b) GND density of the two alloys deformed at 500 °C and different strain rates.

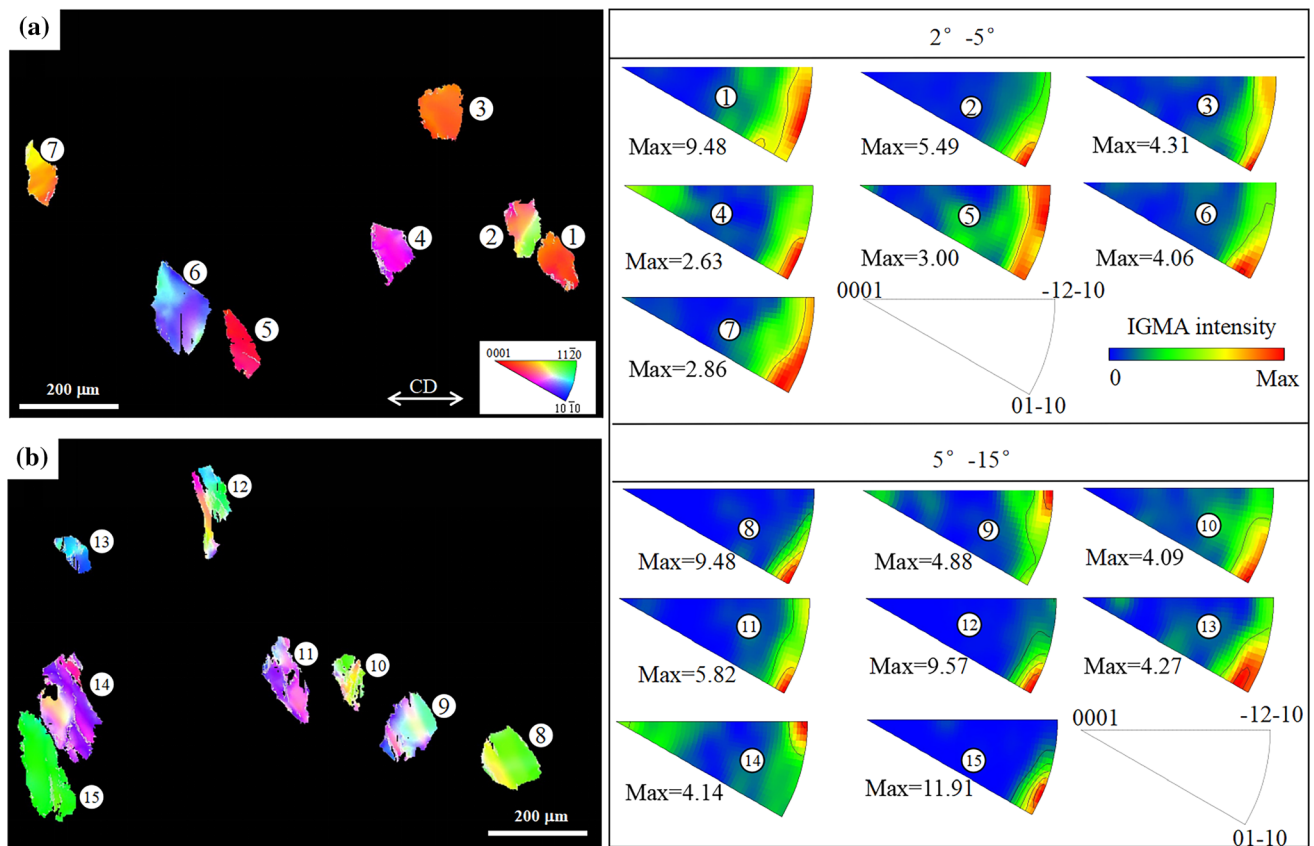


Fig. 15—IGMA analysis of grains in 400AT alloy during 400 °C and 0.001 s⁻¹ compression: (a) IPF map of selected deformed grains 1 to 7 with a misorientation angle between 2 and 5 deg represents the slip mode; (b) IGMA distribution maps of grains 8 to 15 with a misorientation angle between 5 and 15 deg represents the kink mode (Color figure online).

randomly and not located near parent-deformed grains M₃ or M₄, which is due to high local strains extremely changing the lattice orientation, and thus, optimizing the texture.

Besides, a small amount of DRX grain was only found between LPSO phase lamella with relatively wide spacing, and the formation mechanism is discussed by

the TEM results. Figure 18 shows the TEM images of the dislocation walls and DRX grains between LPSO phase lamella in the two alloys under two-beam bright field observation. Dislocation walls and LPSO structures of 400AT alloy under 450 °C/0.001 s⁻¹ compressive are exhibited in Figure 18(a), and the electron beam direction is parallel to ^[11-20] zone axis. According to

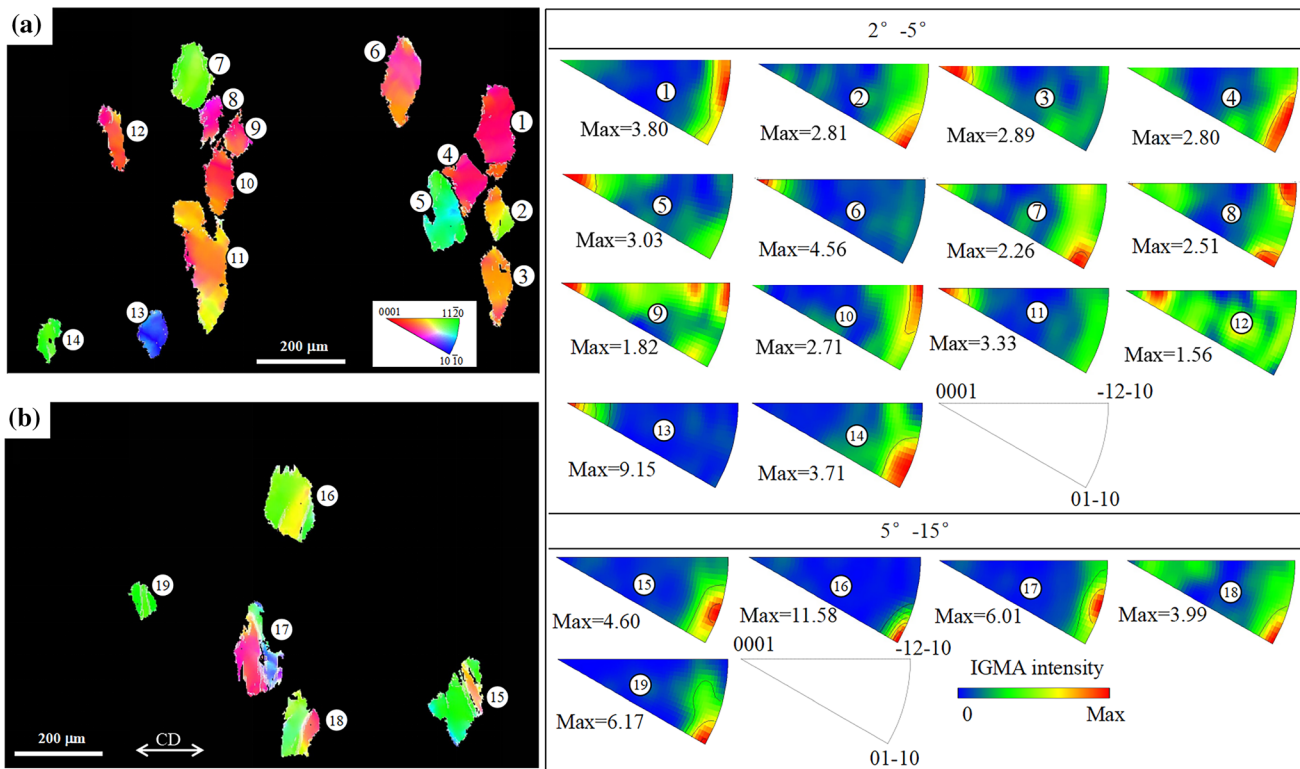


Fig. 16—IGMA analysis of grains in 450AT alloy during 400 °C and 0.001 s⁻¹ compression: (a) IPF map of selected deformed grains 1 to 11 with a misorientation angle between 2 and 5 deg represents the slip mode; (b) IGMA distribution maps of grains 12 to 16 with a misorientation angle between 5 and 15 deg represents the kink mode (Color figure online).

$g \cdot b = 0$ invisibility criteria, the visible dislocation with diffraction vector $g = [0002]$ is $[c]$ containing, which can speculate that $\langle c + a \rangle$ dislocations activate under this compression condition.^[41] In fact, Kim *et al.*^[51] have demonstrated that the deformation mechanism of Mg/LPSO phase is the basal $\langle a \rangle$ slip and pyramidal $\langle c + a \rangle$ slip, and the $\langle c + a \rangle$ pyramidal slip activity is promoted by the elastic modulus mismatch between LPSO phase and α -Mg matrix. However, no DRX grains are observed between the LPSO phase lamella, which is related to the narrow spacing. Figure 18(b) shows the DRX grains located at the kink boundary of LPSO phase in 450AT alloy under 400 °C/0.001 s⁻¹ compression, which coincides with Figure 17(a). In this case, the DRX grains still cannot form between the LPSO phase lamella due to the relatively narrow spacing.

Notably, both the DRX grain between widely spaced LPSO phase lamellae and $\langle c + a \rangle$ dislocation exists in the 450AT alloy under 450 °C/0.001 s⁻¹ compression, as shown in Figure 18(c). According to the above results (Figure 7(c₂)), LPSO phase lamellar spacing gradually increases with the increase of compressive temperature, and enough space provides a favorable condition for the growth of DRX grains. Specifically, when the $\langle c + a \rangle$ dislocations glide on the pyramidal planes, the dense lamellar 14H LPSO phase can effectively hinder their movement, without no DRX grains formation. In contrast, the wide LPSO lamellae space imposes a much weaker constraint on the $\langle c + a \rangle$ dislocations.

The basal $\langle a \rangle$ dislocation that moves parallel to LPSO phase lamellae can entangle with the non-basal dislocations, thereby forming the dislocation walls, and gradually evolving into DRX grains.^[52] Meanwhile, the growth of DRX grains was limited in the space between lamellar 14H LPSO phases, as shown in Figure 18(d).

C. Texture Characteristic

According to the above results and discussion, the $\{0001\}$ and $\{10 - 10\}$ pole figures of the two alloys compressive at 450 °C and 0.001 s⁻¹ were selected to discuss the formation of the texture, as shown in Figure 19. It can be clearly seen that there is a significant difference in the texture between the two alloys. The 400AT alloy possesses a lower texture intensity and random grain orientation (Figures 19(a₁) and (a₂)). On the contrary, for the 450AT alloy (Figures 19(b₁) and (b₂)), the position of pole density peak is approximately perpendicular to CD, which means that the alloy after compression maintains the similar texture to the as-annealed alloy. Based on the DRX mechanism analysis in Figure 17, a large amount of necklace DDRX grains with more random grain orientation is distributed in the 400AT alloy, thereby effectively weakening the texture. However, in the 450AT alloy, on one hand, the stable 14H LPSO phase can release stress concentration by kink deformation and promote the rotation of grain c-axis to the CD. On the other hand, a part of stress is consumed through the formation of CDRX grain

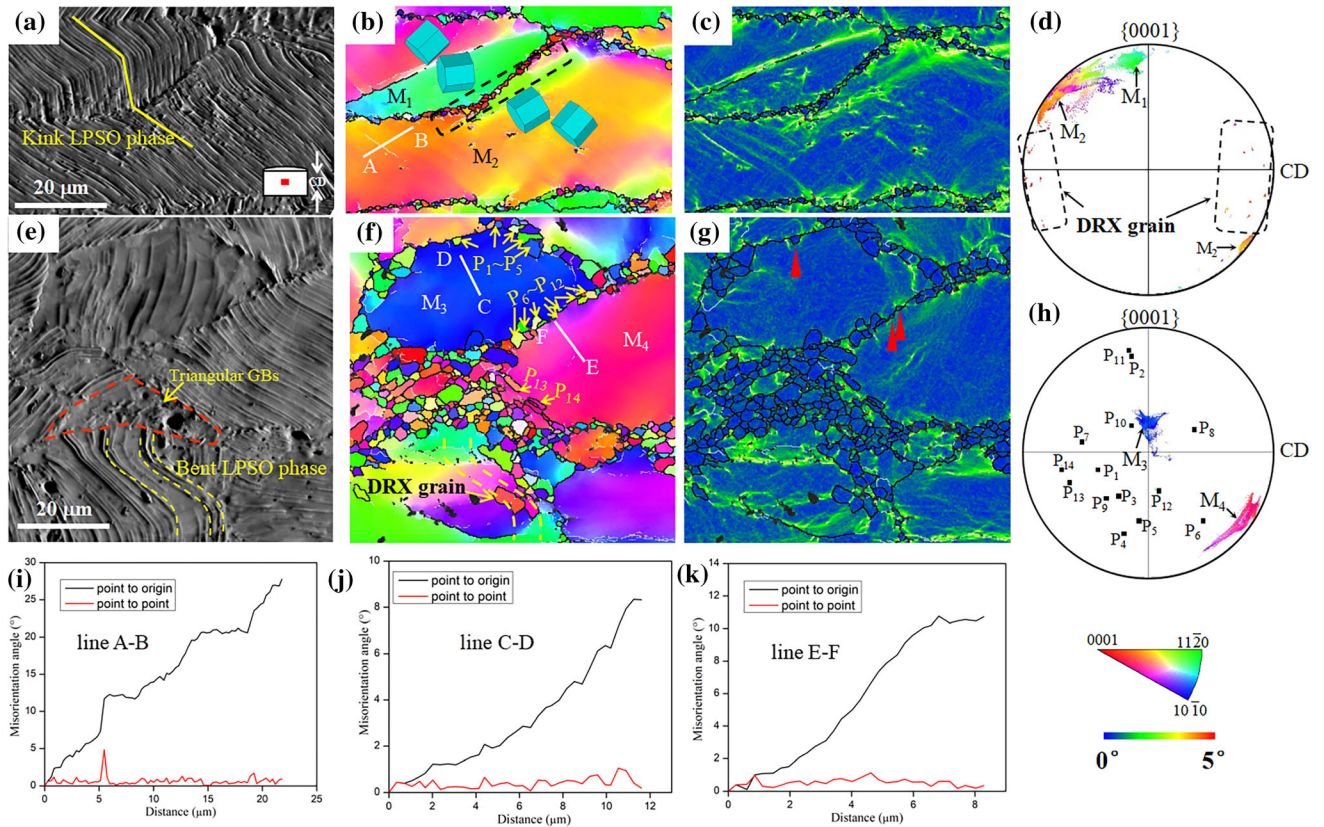


Fig. 17—SEM micrograph, orientation map, KAM map, and $\{0001\}$ scattered data pole figure of DRX grains: (a) through (d) 450AT alloy during $400\text{ }^{\circ}\text{C}/0.001\text{ s}^{-1}$ compression, (e) through (h) 450AT alloy during $450\text{ }^{\circ}\text{C}/0.001\text{ s}^{-1}$ compression. (i) through (k) misorientation profiles along the vector AB, CD, and EF shown in (b) and (f), respectively.

between the wide space of LPSO phase lamellae, which leads to less formation of necklace DDRX grains. Li *et al.* also concluded that the CDRX grains between LPSO phase lamellae have an obvious heritability of orientations, that is to say, the orientations of the DRX grains spread around the orientation of parent-deformed grains.^[53] Here, the effect of CDRX distributed in triangular grain boundaries in both alloys is almost identical in the two alloys, which is due to the PSN mechanism introduced by remaining insoluble block phases during heat treatments. Therefore, the DRX grains formed in 450AT alloy have a limited weakening effect on texture. In addition, as the compression temperature further increases, the degree of re-dissolved LPSO phase in 450AT alloy is higher than that in 400AT alloy. The lamellar 14H LPSO phase gradually transforms into the rod-shaped LPSO phase, which hinders the movement of dislocations and leads to decreases in alloy plasticity. This also corresponds to the plastic destabilization area appearing in the hot processing map of the 450AT alloy (bottom right corner of Figure 6(b)).

V. CONCLUSIONS

In this paper, the hot deformation behavior, microstructure evolution, and DRX mechanism of Mg-4.7Gd-3.4Y-1.2Zn-0.5Zr (wt pct) alloy-containing 14H LPSO phase during hot compression were studied. Two initial microstructures with varied morphology and distribution of LPSO phase were designed by different annealing treatments, which are $400\text{ }^{\circ}\text{C}$ annealed alloy (400AT alloy) and $450\text{ }^{\circ}\text{C}$ annealed alloy (450AT alloy). The main conclusions are drawn as follows:

- (1) The 450AT alloy has sparsely dispersed stable 14H LPSO phases in contrast to the densely distributed metastable 14H LPSO phases in the 400AT alloy. With the compressive temperature increasing or the strain rate decreasing, the 14H LPSO phase morphology in the two alloys produces a quite different change after compressive. In the 400AT alloy, 14H LPSO phase gradually transitions from a metastable state to a stable state accompanied by coarsening and extending. However, in the 450AT alloy, the

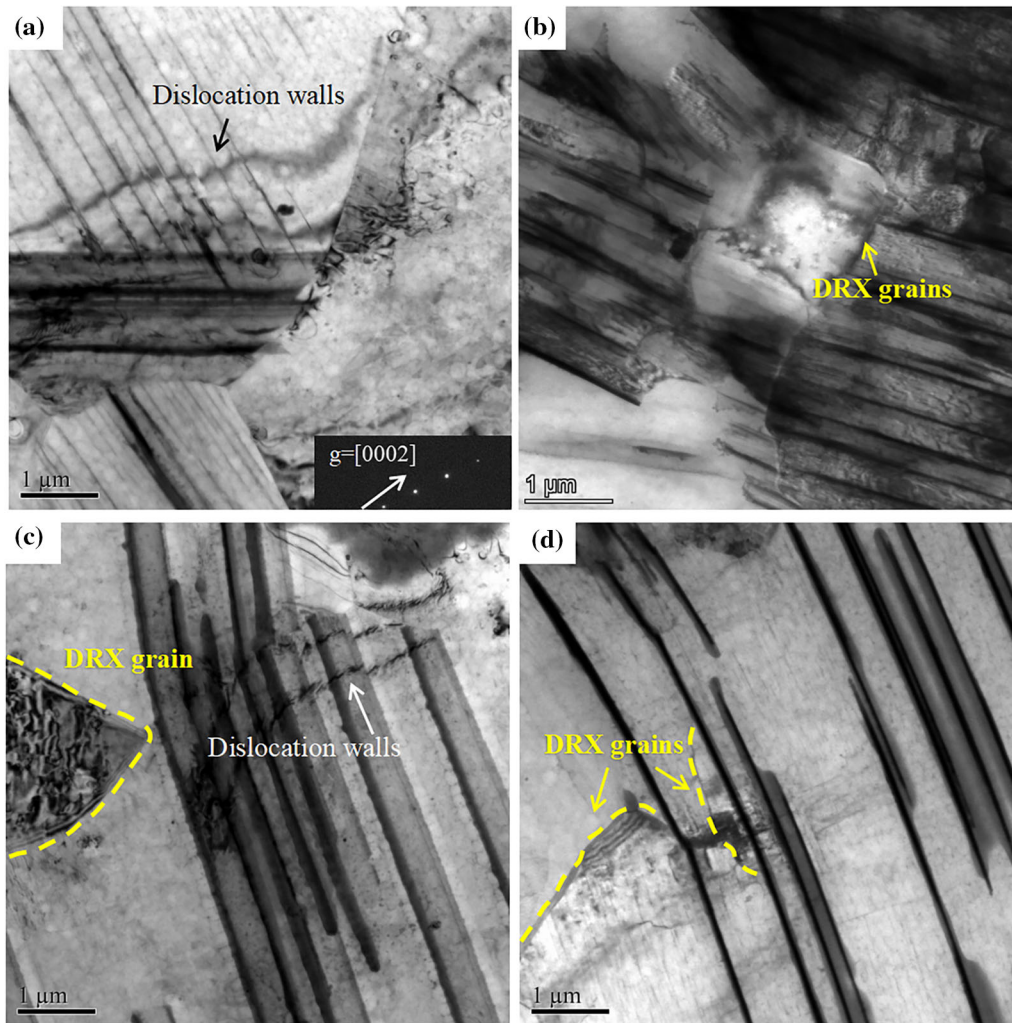


Fig. 18—TEM images of dislocation and DRX grains between LPSO phase lamellae under two-beam bright field observation of (a) 400AT alloy during $450\text{ }^{\circ}\text{C}/0.001\text{ s}^{-1}$ compression, (b) 450AT alloy during $400\text{ }^{\circ}\text{C}/0.001\text{ s}^{-1}$ compression, (c) and (d) 450AT alloy during $450\text{ }^{\circ}\text{C}/0.001\text{ s}^{-1}$ compression.

14H LPSO phase gradually re-dissolved along with coarsening and shortening.

- (2) The peak stress and activation energy Q value of the 400AT alloy (254.2 kJ/mol) is approximates that of the 450AT alloy (257.7 kJ/mol), and the 400AT alloy has a broader suitable hot processing window than the 450AT alloy. The Portevin–Le Chatelier phenomenon presented in the 400AT alloy compressive at $400\text{ }^{\circ}\text{C}$ and 0.1 s^{-1} , while it occurred in the 450AT alloy during $450\text{ }^{\circ}\text{C}$ and 0.1 s^{-1} compression. This is attributed to the interaction between the movable dislocations and

solute atoms produced by the variation of 14H LPSO phase morphology.

- (3) The discontinuous dynamic recrystallization (DDRX) and continuous dynamic recrystallization (CDRX) were existed simultaneously in both alloys during hot compression. The necklace-shaped DDRX grain was mainly distributed around the original deformed grains, while CDRX grain was primarily located in the kink boundary, triangular grain boundary, and widely spaced LPSO phase lamella. In the 450AT alloy, CDRX grains form in more 14H LPSO phase

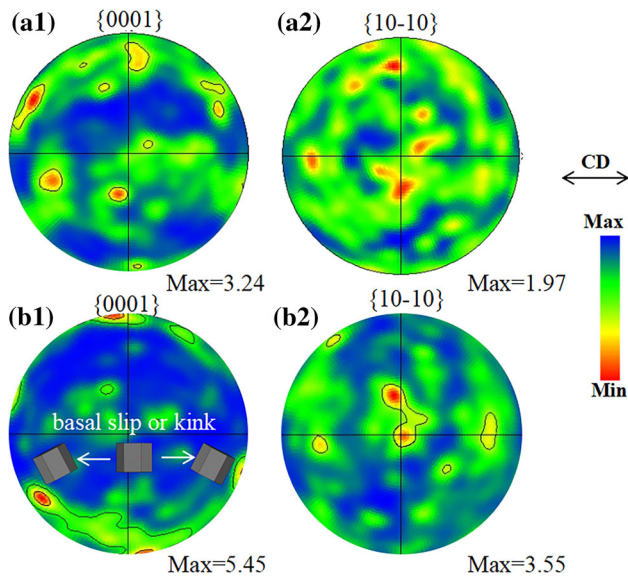


Fig. 19—{0001} and {11-20} pole figures of the two alloys compressive at 0.001 s^{-1} and $450\text{ }^{\circ}\text{C}$ (a_1) and (a_2) 400AT alloy, (b_1) and (b_2) 450AT alloy.

kink boundary and between the wide space of LPSO phase lamellae, which have a limited weakening effect of texture. The 400AT alloy has a weaker texture intensity and more randomly distributed grain orientation compared with the 450AT alloy, which was related to the large amount of DDRX grains. The weak basal texture effectively improves the hot workability of the alloy and fits well with the wider hot processing window of 400 AT alloy.

ACKNOWLEDGMENTS

The authors acknowledge the financial support from the Key Research and Development Project of Hunan Province (No. 2023GK2020).

CONFLICT OF INTEREST

On behalf of all authors, the corresponding author states that there is no conflict of interest.

REFERENCES

1. M. Matsushita, K. Masuda, R. Waki, H. Ohfuji, M. Yamasaki, Y. Kawamura, and Y. Higo: *J. Alloys Compd.*, 2019, vol. 784, pp. 1284–89.
2. B.L. Mordike and T. Ebert: *Mater. Sci. Eng. A*, 2001, vol. 302, pp. 37–45.
3. G.L. Bi, D.Q. Fang, W.C. Zhang, J. Sudagar, Q.X. Zhang, J.S. Lian, and Z.H. Jiang: *J. Mater. Sci. Technol.*, 2012, vol. 28, pp. 543–51.
4. Y. Kawamura, K. Hayashi, A. Inoue, and T. Masumoto: *Mater. Trans.*, 2001, vol. 42, pp. 1172–76.
5. L.Y. Feng, X.X. Dong, Q. Cai, B. Wang, and S.X. Ji: *J. Alloys Compd.*, 2019, vol. 793, 166364.

6. J.S. Zhang, C. Xin, W.L. Cheng, L.P. Bian, H.X. Wang, and C.X. Xu: *J. Alloys Compd.*, 2013, vol. 558, pp. 195–202.
7. C. Xu, M.Y. Zheng, S.W. Xu, K. Wu, E.D. Wang, S. Kamado, G.J. Wang, and X.Y. Lv: *Mater. Sci. Eng. A*, 2012, vol. 547, pp. 93–98.
8. S.M. Ramezani, A. Zarei-Hanzaki, H.R. Abedi, A. Salandari-Rabori, and P. Minarik: *J. Alloys Compd.*, 2019, vol. 793, pp. 134–45.
9. H. Okuda, T. Horiuchi, S. Hifumi, M. Yamasaki, Y. Kawamura, and S. Kimura: *Metall. Mater. Trans. A*, 2014, vol. 45A, pp. 4780–785.
10. Y. Tang, Q.C. Le, R.D.K. Misra, G.Q. Su, and J.Z. Cui: *Mater. Sci. Eng. A*, 2018, vol. 712, pp. 266–80.
11. C. Xu, M.Y. Zheng, K. Wu, E.D. Wang, G.H. Fan, S.W. Xu, S. Kamado, X.D. Liu, G.J. Wang, and X.Y. Lv: *Mater. Sci. Eng. A*, 2013, vol. 559, pp. 615–22.
12. X.J. Zhou, C.M. Liu, Y.H. Gao, S.N. Jiang, X.Z. Han, and Z.Y. Chen: *Metall. Mater. Trans. A*, 2017, vol. 48A, pp. 3060–72.
13. G. Liu, Z.D. Ma, G.B. Wei, T.C. Xu, X. Zhang, Y. Yang, W.D. Xie, and X.D. Peng: *J. Mater. Process. Technol.*, 2019, vol. 267, pp. 393–402.
14. H. Somekawa and D. Ando: *Mater. Sci. Eng. A*, 2020, vol. 780, 139144.
15. C.R. Liu, L. Li, W. Zhou, X. Bai, H.L. Zhong, Z.Q. Zhang, and Z.Z. Wen: *J. Alloys Compd.*, 2023, vol. 937, 168356.
16. K. Hagihara, T. Mayama, M. Honnami, M. Yamasaki, H. Izuno, T. Okamoto, T. Ohashi, T. Nakano, and Y. Kawamura: *Int. J. Plasticity*, 2016, vol. 77, pp. 174–91.
17. M. Yamasaki, K. Hagihara, S. Inoue, J.P. Hadorn, and Y. Kawamura: *Acta Mater.*, 2013, vol. 61, pp. 2065–76.
18. E. Oñorbe, P. Pérez Zubiaur, G. Garcés, and P. Adeva: *J. Mater. Sci.*, 2012, vol. 47, pp. 1085–93.
19. G.X. Wang, P.L. Mao, Z. Wang, L. Zhou, F. Wang, and Z. Liu: *J. Mater. Res. Technol.*, 2022, vol. 21, pp. 40–53.
20. J.H. Zhang, S.J. Liu, R.Z. Wu, L.G. Hou, and M.L. Zhang: *J. Magnes. Alloy.*, 2018, vol. 6, pp. 277–91.
21. J.B. Lyu, J. Kim, H.X. Liao, J. She, J.F. Song, J. Peng, F.S. Pan, and B. Jiang: *Mater. Sci. Eng. A*, 2020, vol. 773, 138735.
22. G. Garcés, D.G. Morris, M.A. Muñoz-Morris, P. Perez, D. Tolnai, C. Mendis, A. Stark, H.K. Lim, S. Kim, N. Shell, and P. Adeva: *Acta Mater.*, 2015, vol. 94, pp. 78–86.
23. Y. Chino, M. Mabuchi, S. Hagiwara, H. Iwasaki, A. Yamamoto, and H. Tsubakino: *Scr. Mater.*, 2004, vol. 51, pp. 711–14.
24. M. Li, X. Wang, Q.Y. Feng, J. Wang, Z. Xu, and P.H. Zhang: *Mater. Charact.*, 2017, vol. 125, pp. 123–33.
25. X. Wu, F.S. Pan, R.J. Cheng, and S.Q. Luo: *Mater. Sci. Eng. A*, 2018, vol. 726, pp. 64–68.
26. Y.F. Wang, F. Zhang, Y.T. Wang, Y.B. Duan, K.J. Wang, W.J. Zhang, and J. Hu: *Mater. Sci. Eng. A*, 2019, vol. 745, pp. 149–58.
27. B.J. Lv, J. Peng, L.L. Zhu, Y.J. Wang, and A.T. Tang: *Mater. Sci. Eng. A*, 2014, vol. 599, pp. 150–59.
28. D.X. Zhang, Z. Tan, Q.H. Huo, Z.Y. Xiao, Z.W. Fang, and X.Y. Yang: *Mater. Sci. Eng. A*, 2018, vol. 715, pp. 389–403.
29. C. Xu, T. Nakata, X. Qiao, M. Zheng, K. Wu, and S. Kamado: *Sci. Rep.*, 2017, vol. 7, pp. 1–10.
30. J.X. Xiao, Z.Y. Chen, J.B. Shao, T. Chen, X. Lin, and C.M. Liu: *Mater. Charact.*, 2020, vol. 167, 110515.
31. Y.X. Han, S.H. He, T. Chen, J.B. Shao, C.M. Liu, Z.Y. Chen, and Z. Yang: *Mater. Sci. Eng. A*, 2022, vol. 856, 144002.
32. T. Chen, Z.Y. Chen, J.B. Shao, and R.K. Wang: *Mater. Sci. Eng. A*, 2019, vol. 750, pp. 31–39.
33. T. Chen, Z.Y. Chen, J.B. Shao, R.K. Wang, L.H. Mao, and C.M. Liu: *Mater. Des.*, 2018, vol. 152, pp. 1–9.
34. J.K. Kim, W.S. Ko, S. Sandlöbes, M. Heidelmann, B. Grabowski, and D. Raabe: *Acta Mater.*, 2016, vol. 112, pp. 171–83.
35. H. Liu, K. Yan, J.L. Yan, F. Xue, J.P. Sun, J.H. Jiang, and A.B. Ma: *Trans. Nonferrous Met. Soc.*, 2017, vol. 27, pp. 63–72.
36. Y.M. Zhu, A.J. Morton, and J.F. Nie: *Acta Mater.*, 2010, vol. 58, pp. 2936–47.
37. Z.C. Sun, H.L. Wu, J. Cao, and Z.K. Yin: *Int. J. Plasticity*, 2018, vol. 106, pp. 73–87.
38. J.R. Kang, X. Liu, and T.Z. Wang: *Scr. Mater.*, 2023, vol. 224, 115121.
39. L.H. Li, F.G. Qi, Q. Wang, C.H. Hou, N. Zhao, Y. Yang, S.S. Chai, and X.P. Ouyang: *Mater. Charact.*, 2020, vol. 169, 110649.

40. X.J. Zhou, C.M. Liu, Y.H. Gao, S.N. Jiang, W.H. Liu, and L.W. Lu: *J. Alloys Compd.*, 2017, vol. 724, pp. 528–36.
41. B.J. Lv, J. Peng, Y. Peng, A.T. Tang, and F.S. Pan: *Mater. Sci. Eng. A*, 2013, vol. 579, pp. 209–16.
42. A. Hadadzadeh, F. Mokdad, M.A. Wells, and D.L. Chen: *Mater. Sci. Eng. A*, 2018a, vol. 709, pp. 285–89.
43. M. Calcagnotto, D. Ponge, E. Demir, and D. Raabe: *Mater. Sci. Eng. A*, 2010, vol. 527, pp. 2738–46.
44. Y.B. Chun, M. Battaini, C.H.J. Davies, and S.K. Hwang: *Metall. Mater. Trans. A*, 2010, vol. 41A, pp. 3473–87.
45. Y. Yao, C.M. Liu, Y.C. Wan, S.L. Yu, Y.H. Gao, and S.N. Jiang: *Mater. Charact.*, 2020, vol. 161, p. 1110120.
46. X.H. Shao, Z.Q. Yang, and X.L. Ma: *Acta Mater.*, 2010, vol. 58, pp. 4760–71.
47. J.Y. Li, F.L. Wang, J. Zeng, C.Y. Zhao, L. Jin, and J. Dong: *Mater. Charact.*, 2022, vol. 193, p. 112326.
48. D.F. Zheng, Q.C. Zhu, X.Q. Zeng, and Y.X. Li: *Mater. Lett.*, 2022, vol. 311, p. 131524.
49. L.S. Toth, Y. Estrin, R. Lapovok, and C.F. Gu: *Acta Mater.*, 2010, vol. 58, pp. 1782–94.
50. D.H. Qin, M.J. Wang, C.Y. Sun, Z.X. Su, L.Y. Qian, and Z.H. Sun: *Mater. Sci. Eng. A*, 2020, vol. 788, p. 139537.
51. J.K. Kim, S. Sandlöbes, and D. Raabe: *Acta Mater.*, 2015, vol. 82, pp. 414–23.
52. A. Galiyev, R. Kaibyshev, and G. Gottstein: *Acta Mater.*, 2001, vol. 49, pp. 1199–1207.
53. D.D. Zhang, C.M. Liu, S.N. Jiang, Y.H. Gao, Y.C. Wan, and Z.Y. Chen: *J. Alloys Compd.*, 2023, vol. 944, p. 169190.

Publisher's Note Springer Nature remains neutral with regard to jurisdictional claims in published maps and institutional affiliations.

Springer Nature or its licensor (e.g. a society or other partner) holds exclusive rights to this article under a publishing agreement with the author(s) or other rightsholder(s); author self-archiving of the accepted manuscript version of this article is solely governed by the terms of such publishing agreement and applicable law.